

Identifying Chemical Factors Affecting Reaction Kinetics in Li-air Battery via *ab initio* Calculations and Machine Learning

Aiping Wang^a, Zheyi Zou^a, Da Wang^a, Yue Liu^b, Yajie Li^a, Junming Wu^b, Maxim Avdeev^{c,d}, Siqi Shi^{a,e,*}

^a State Key Laboratory of Advanced Special Steel, Shanghai Key Laboratory of Advanced Ferrometallurgy, School of Materials Science and Engineering, Shanghai University, Shanghai 200444, China

^b School of Computer Engineering and Science, Shanghai Institute for Advanced Communication and Data Science, Shanghai University, Shanghai 200444, China

^c Australian Nuclear Science and Technology Organisation, Locked Bag 2001, Kirrawee DC NSW 2232, Australia

^d School of Chemistry, The University of Sydney, Sydney 2006, Australia

^e Materials Genome Institute, Shanghai University, Shanghai 200444, China

ABSTRACT

Redox mediators are promised to thermodynamically resolve the cathode irreversibility of Li-air battery. However, the sluggish chemical reaction between mediators and discharge products severely restrains fast charging. Here, we combine *ab initio* calculations and machine learning method to investigate the reaction kinetics between LiOH and I₂, and demonstrate the critical role of the disorder degree of LiOH and the solvent effect. The Li⁺ desorption is identified as the *rate determining step* (rds) of the reaction. While LiOH turns from the crystalline to disordered/amorphous structure, the rds energy barrier will be reduced by ~500 meV. The functional group of the solvent is detected as the key to regulating the solvation effect and phosphate-based solvent is predicted to accelerate the decomposition kinetics most with the strongest solvation capability. These findings indicate that the faster reaction kinetics between mediators and the discharge products can be achieved by rational discharge product structure regulation and appropriate solvent selection.

1. Introduction

Li-air battery has attracted enormous attention due to its considerably higher theoretical energy density than that of most of the other battery chemistries. However, the poor reversibility and sluggish oxygen evolution reaction (OER) have impeded the practical utilization of the promised capacity, leading to the extremely low round-trip efficiency and cycle life [1]. The introduction of redox mediators (RM) that serve as novel soluble catalysts with flexible mass transport ability and admirable cyclability has emerged as an effective strategy to resolve these hurdles [2–4]. In the charging process, the RM operates in two steps: (i) its electrochemical oxidation, generating RM⁺, and (ii) its regeneration via the oxidation of discharge products by RM⁺ [5]. A small gap between the redox potential of the RM and that of the theoretical cathode reaction is desired to achieve the high efficacy (Fig. 1) [5].

Whilst a bright prospect is promised by the RMs, their slow kinetics remains to be a hurdle to application, and the detailed reaction mechanism is poorly understood [6,7]. Generally, the kinetics concerning RM can be classified into three categories: (1) *electrochemical* that relies on the electron transfer between RM and the electrode; (2) *diffusional* where RM has to transport from the electrode to the discharge products; and (3) *chemical* reaction directly between the RM and the discharge products. Reports have been available for each category. The sluggish reaction can cause the abnormal high-potential (~3.2 V vs. Li/Li⁺) in the discharge

process [3,7–10], which can be attributed to the steric structure of the RM [6], the oxidation state and mass diffusivity of the RM [11], as well as the activity of the discharge products [7].

However, not only the steric hindrance of RM [6], but also the structure of the discharge product and the solvent [11] play critical roles in regulating the OER reaction kinetics. Both the experimental and theoretical studies show that the discharge product structures directly affect the charging reaction kinetics [12–15]. With the help of *in operando* X-ray diffraction, the non-stoichiometric Li(OH)_{1-x} has been found to decompose prior to the stoichiometric structure [16]. The high index surfaces were also calculated to decompose easier than the low index surfaces [12,13]. Concerning the electrolyte, higher discharge potential was found to be correlated with the donor number (DN) of the solvents, which is a quantitative measure of the Lewis basicity [17]. Proton activity of the solvent was shown to increase the reaction kinetics between RM and the discharge products [14]. Yet, there is still no general understanding of different disordered discharge products as well as the solvation effect on the OER kinetics in Li-air battery.

Additional problems are related to the proton-contaminated electrolyte or cathodic active materials, typically, H₂O leads to the discharge products of LiOH [10,18–22]. The deprotonation of H₂O was reported to be easier when incorporating RM lithium iodide (LiI) into the electrolyte [22–24]. LiI, a simple inorganic RM, has been widely and successfully used in the pursuit of a Li-air battery with impressive performance

* Corresponding author

E-mail address: sqshi@shu.edu.cn (S. Shi).

<https://doi.org/10.1016/j.ensm.2020.10.022>

Received 9 August 2020; Received in revised form 30 September 2020; Accepted 26 October 2020

Available online 28 October 2020

2405-8297/© 2020 Elsevier B.V. All rights reserved.

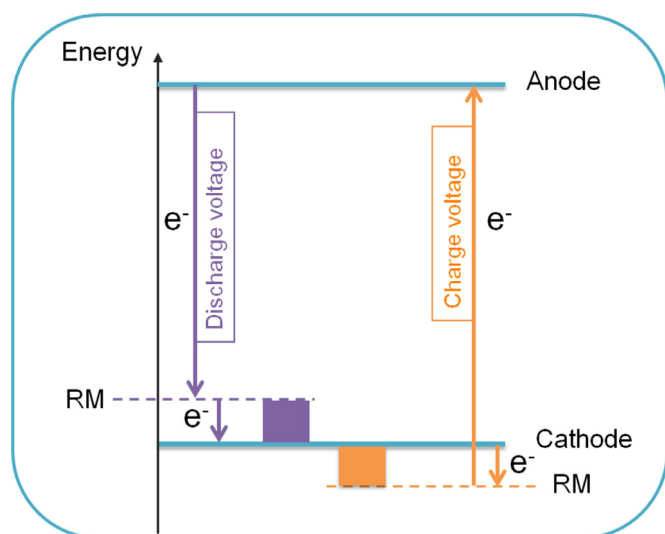


Fig. 1. A schematic for the mechanism of the RM in the battery cycle. The theoretical potentials of both electrodes are signified with two bolded lines. The redox potentials of RM are noted with two dashed lines, purple for the discharge RM and orange for the charge RM, locating at both sides of the theoretical cathode potential. The arrows are the electron-flow processes during charge and discharge, which constitute a full discharge/charge cycle. During charge, the electron flows from the lower level of RM to the anode energy level, reducing the anode active materials, e.g., Li^+ , and then the electron in the discharge product flows to the hole in the RM^+ , which possesses a lower energy level. The discharge product is oxidized. During discharge, the electron flows from the high energy level of the anode, reducing the RM, and then the electron in the RM^- flows to cathode active materials, e.g., O_2 , which possesses a lower energy level, forming the discharge product.

[8,10,16,18,20,24]. The reversible LiOH formation and decomposition have been observed by the *in operando* X-ray diffraction when LiI was added as the RM [16].

Herein, using *ab initio* calculations and machine learning, which have been extensively used to explore the battery chemistry [25], we unravel the discharge product structure effect and solvation effect on the OER reaction kinetics between RM (LiI) [8,18,20,26] and the discharge products (LiOH). The LiI and LiOH are selected due to the simple structure and the promising discharge products with multiple electron electrochemistry, respectively. The investigation of the elementary reaction identifies Li^+ desorption as the *rate determined step* (rds) in the chemical reaction, whose energy barrier can be reduced by ~ 500 meV when LiOH turns from the ideally crystalline to the disordered/amorphous structure. The comparison of the solvation effects of 33 solvents on the rds shows that the functional group of the solvent molecule serves as the key to regulating the solvation capability. Based on such understanding, the phosphate-based solvent is predicted to offer the most efficient LiOH decomposition kinetics.

2. Results and Discussion

It is known that the OER process with RM includes the electrochemical and chemical processes. Firstly, we consider the electrochemical process, the oxidation of the iodine species, where the redox couples I^-/I_3^- and I_3^-/I_2 are concerned using the thermodynamic cycle in Fig. S7. The optimized geometries of the iodine species are shown in Fig. S1. Table 1 shows the calculated redox potentials, in agreement with the experimental values [14,20]. Also, the results calculated by the direct method [27] are listed in Table S1, which also shows the general trend of the potential.

With RM present, the second step of the OER process is a chemical reaction, i.e., the oxidation of the discharge product LiOH by the oxidized

Table 1

Redox potentials of the iodine species. The abbreviations, Cal. and Exp., denote the calculated and experimental values, respectively.

Redox couple	Redox potential (V vs. Li/Li^+)		
	Cal. ^a	Exp. [20]	Exp. [14]
I^-/I_3^-	3.37	3.2	3.28
I_3^-/I_2	3.89	3.7	3.60

^a The optimization of all geometries were conducted at the M06-L/ Stuttgart level and the solvation energy calculation were conducted at the M05-2X/ Stuttgart level.

RM. As a start, we begin the theoretical calculation from the decomposition of the crystalline LiOH and determined an optimized reaction path. The low index surfaces (001) and (100) [13] are considered and three reaction paths are comprehensively investigated. The reaction processes of all the three reaction paths are described detailed in the Section S1.3 of the Supplementary Information (SI) and the corresponding relative reaction energies (E_r) are presented in Table S2. All the reactions start from the attack of I rather than the I_2 to the exposed LiOH surface as the energy difference between I_2^* and I^* (* denotes the adsorbed species), as shown in Fig. S2, on the reaction surface is much lower than the rds reaction energy (E_r). If there are more than one LiI in the reaction surface, the priority of the detachment of these LiI will be tested and the most stable system after the desorption will be determined as the favorable product.

Fig. 2 presents the surface models and the reaction energy of the rds for different paths conducted in the (001) and (100) surfaces of LiOH, respectively. Combined the anatomized reaction equations and the reaction energetics, the desorption of LiI is determined as the rds of the LiOH decomposition and the rds E_r are shown in Fig. 2c and 2d. It is noted path 3 has the lowest rds for both (001) and (100) surfaces. And path 1 is also possible for the (100) surface due to the comparable E_r . Here we select path 3 to further investigate the decomposition of the disordered/amorphous model as the structure disordering is the only variable during the exploration of the structural effect. According to the reaction energetics, the non-stoichiometric (100) surface is found more reactive than the stoichiometric (001) surface, in agreement with the electrochemical reaction process for both LiOH [13] and Li_2O_2 [12]. It is noted that all the reaction energetics presented in Table S2 are the relative E_r with respect to the rds E_r of path 3 conducted in the disordered/amorphous surface.

To further confirm the reaction activity of different disordered structures, we explore the electronic structure [28,29] on typical structures prior the rds reaction. Fig. S3 shows the projected density of states (PDOS) of the specific structure prior rds reaction for different paths performed in different surfaces. As for (001) surface, the hybridization energy levels (E_{hyb} , noted with dashed purple line) between the desorbed LiI and the oxygen in the LiOH matrix shifts up from path 1 (Fig. S3a) to path 3 (Fig. S3c) by 2.72 eV, indicating the weaker orbital hybridization between LiI and the LiOH matrix in the path 3 reaction. Also, for the paths performed in (100) surface, the path 3 (Fig. S3f) has the highest E_{hyb} , viz., the weakest hybridization. The weaker hybridization of the structure for path 3 is consistent with the lower E_r of it.

To investigate the effect of the structure disorder on the chemical reaction, structures with different degree of disordering are taken into account. A structural disorder parameter, α , based on the Li–O bond length deviation with respect to the ideal crystal structure, is defined to quantitatively describe the disordering extent and to give a visual concept of the correlation between the disordering extent and the rds E_r as:

$$\alpha = \frac{2\sqrt{\sum_{i=1}^n (d_i - d_0)^2}}{n} \quad (1)$$

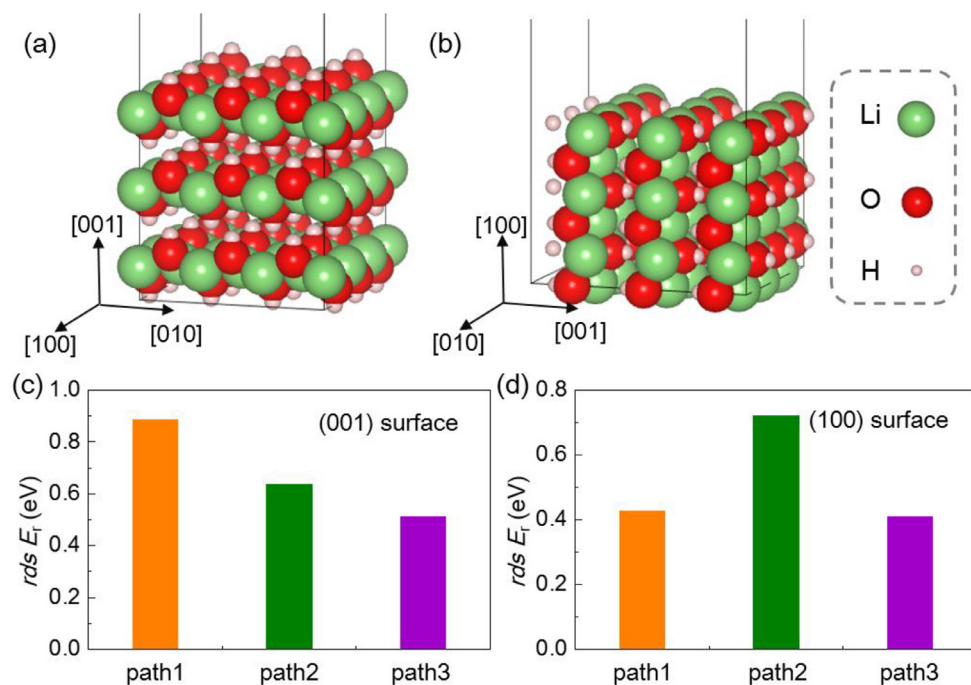


Fig. 2. (a) and (b) are the surface of models of (001) and (100) surfaces; (c) and (d) are the respective rds reaction energy ($rds E_r$) extracted from different paths for the decomposition of these two surfaces. The path 3 has the lowest $rds E_r$ among the three paths for both surfaces.

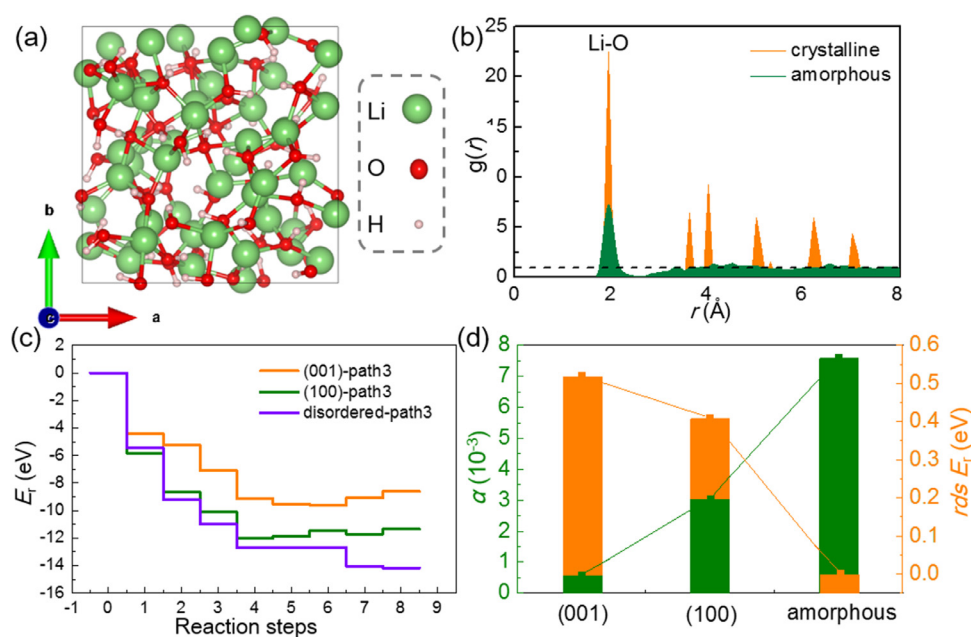


Fig. 3. (a) The disordered/amorphous LiOH model; (b) The radial distribution function of both the crystalline and the disordered/amorphous model of LiOH; (c) The reaction energetics of path 3 for different surface models; (d) The disordering parameters for different surface models, (001), (100) and disordered/amorphous, as well as their $rds E_r$.

where α is the extent of the disorder, d_i and d_0 are the Li–O bond lengths of the structure studied and the perfect crystalline structure, respectively, d_0 is 1.94775 Å, n is the number of the Li–O bond in a structure. To exclude the thickness effect which will reduce the disorder parameter in the crystalline structures, only the Li–O bonds which are free to relax during the optimization are taken into account. According to the definition above, the higher the value of α is, the more disordered the model is.

Apart from the (001) and (100) surface models mentioned above, an disordered/amorphous surface model (Fig. 3a) is also constructed, which is observed in the experiment [30]. To confirm the disordering, the radial distribution functions (RDF, $g(r)$) of the Li–O coordination are calculated for both the crystalline and disordered/amorphous models for comparison, as shown in Fig. 3b. The $g(r)$ of the dis-

ordered/amorphous model indicates a long-range disorder and the integrations of the first peak within 3 Å of the crystalline and amorphous model are 2.2 and 2.1, respectively, suggesting the comparable coordination number of the oxygen around lithium for both models.

To compare the reaction activity of different models which have different disordering extent, path 3 was used to perform on the disordered/amorphous surface model. The afore-defined disordering parameter (α) of different models was calculated. Fig. 3c gives the reaction energetics for path 3 of all three surface models, which shows that the disordered model is the most reactive. To present the activity difference more clearly, the $rds E_r$ of different models was extracted and plotted in Fig. 3d (the orange line) as well as the disordering parameter (α) (the green line). As expected, the (100) surface model, whose surface layer is non-stoichiometric as $\text{Li}(\text{OH})_{3/4}$, is more disordered than the (001)

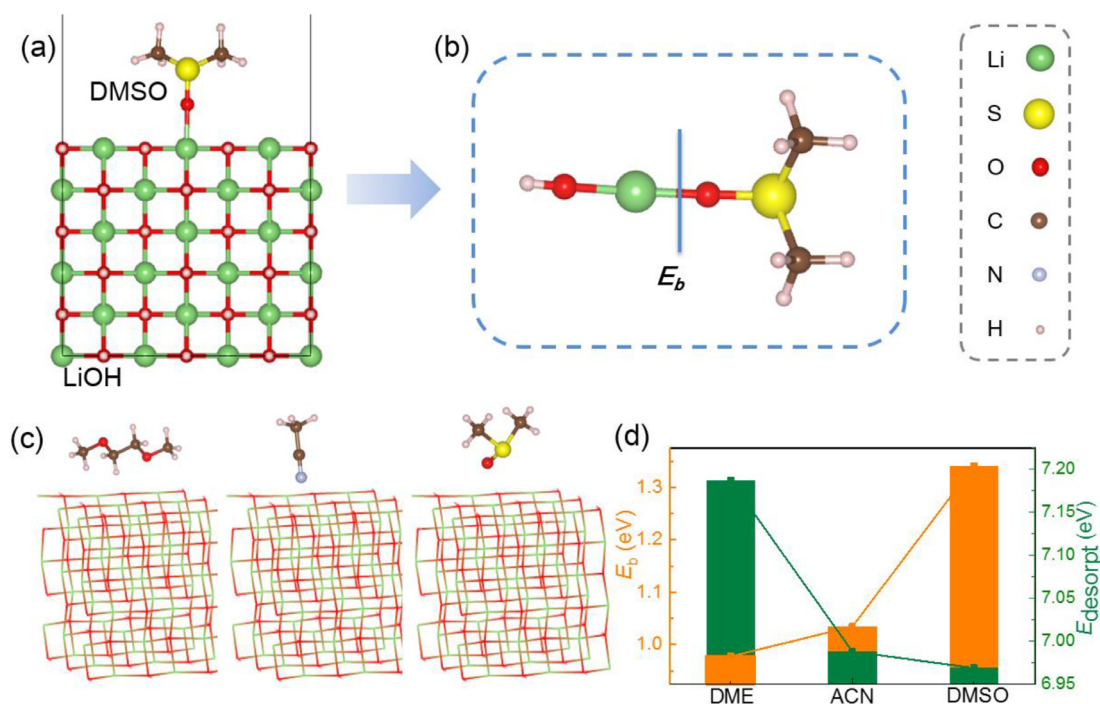


Fig. 4. Schematics to illustrate the solvent effect: (a) the model considering the reaction surface; (b) the model considering single LiOH molecule; (c) geometries for the adsorption of three common solvent molecules on the LiOH surface; (d) the E_b calculated from model (b) for different solvent molecules and the trend of $E_{desorpt}$ of the lithium in the LiOH surface when binding to the solvent molecule as shown in (c).

surface model, and correspondingly, the (100) surface model is more reactive, consistent with the *in operando* X-ray diffraction study [16]. The *rd*s E_r of the disordered/amorphous model is 500 meV lower than that of the (001) surface, which translates into reaction rate constant as:

$$k = e^{-E_a/RT} \quad (2)$$

where E_a is the *rd*s E_r in the reaction process, R and T are the gas constant and temperature, respectively. The rate constant of the disordered/amorphous structure can speed up $\sim 2.8 \times 10^8$ times than that of the crystalline (001) structure at 298.15 K. In experiment, when appropriate catalyst is used, the structurally disordered/amorphous discharge product can be obtained that leads to easier decomposition on charging [31,32].

The above reaction energetics exploration has shown that the reactivity is different for different disordered systems. To further examine the origins of the different reactivity for different disordered models, the total density of states (TDOS) of which are calculated, as shown in Fig. S4. The disordered/amorphous surface model possesses the highest E_F (0.950 eV) than that of the (001) and (100) surfaces, the E_F of the latter two crystalline surfaces are 0 eV. The more energetic electron activity explains the highest reactivity of the disordered/amorphous surface. Though the E_F of the two crystalline surfaces, (001) and (100), are the same, the second occupied states peak of the (100) surface is 1.09 eV higher than that of the (001) surface model, demonstrating the more energetic electron activity of the (100) surface. The electronic structure analysis further confirms that the more disordered/amorphous the structure is, the more active it is.

The decomposition of LiOH is complicated as it is a multi-phase reaction. The solvent has been demonstrated to mediate the active mass transfer and determine the reaction kinetics [33,34]. To approach the practical battery system, we consider the solvation effect of 33 solvents on the chemical reaction kinetics. As demonstrated in the above reaction processes, LiI desorption is the *rd*s of the decomposition in the chemical reaction between LiOH and I_2 . Herein, the solvation effect is focused on

the solvation energetics of LiI and used to screen out the specific solvent which facilitates the reaction kinetics most.

Firstly, we assess the solvation significance to both Li^+ and I^- by considering four common solvents using the SMD implicit solvation models. And the first solvation shell of Li^+ is considered. The solvation free energy of the two species are shown in Table S3. It is found that the solvation free energy of I^- is one third of that for Li^+ . Also, the solvation energies of I^- in different solvents are less distinguishable than that of Li^+ . Thus, only the solvent effect on Li^+ is considered in the follow-up study.

Fig. 4 clarifies a simple and predictive model of the solvation effect and aims to screen out the appropriate solvent for faster OER reaction kinetics. Fig. 4a schematically gives the initial solvating process, the active center of the solvent molecule defined in the SI is bonded to the Li^+ which is about to detach, with the (100) surface and the dimethyl sulfoxide (DMSO) molecule as an example. The initial solvation effect is suggested by the desorption energy ($E_{desorpt}$) of the Li^+ , defined as:

$$E_{desorpt} = E(mol \cdots Li^+) + E(Li_{n-1}(OH)_n^-) - E(mol \cdots (LiOH)_n) \quad (3)$$

where $E(mol \cdots Li^+)$, $E(Li_{n-1}(OH)_n^-)$ and $E(mol \cdots (LiOH)_n)$ are the DFT energy of the systems and *mol* represents the solvent molecule, n is the number of LiOH formula in the system.

To avoid the complex interference of the van der Waals interaction and the hydrogen bonding between the surface and the solvent molecule, the model in Fig. 4a is transformed to Fig. 4b only considering the binding energy (E_b) between the LiOH and the solvent molecule by:

$$E_b = -(E_{(LiOH \cdots mol)} - E_{LiOH} - E_{mol}) \quad (4)$$

where E is the energy of the species and the subscript *mol* represents the solvent molecule.

To transform the model in Fig. 4a to Fig. 4b, the consistency has to be confirmed first. The solvation effect of three common solvents (dimethoxy ethane, acetonitrile and DMSO) are considered with both models in Fig. 4a and 4b. Fig. 4c gives the practical models of these solvents on the LiOH surface. The practical systems of the schematic in

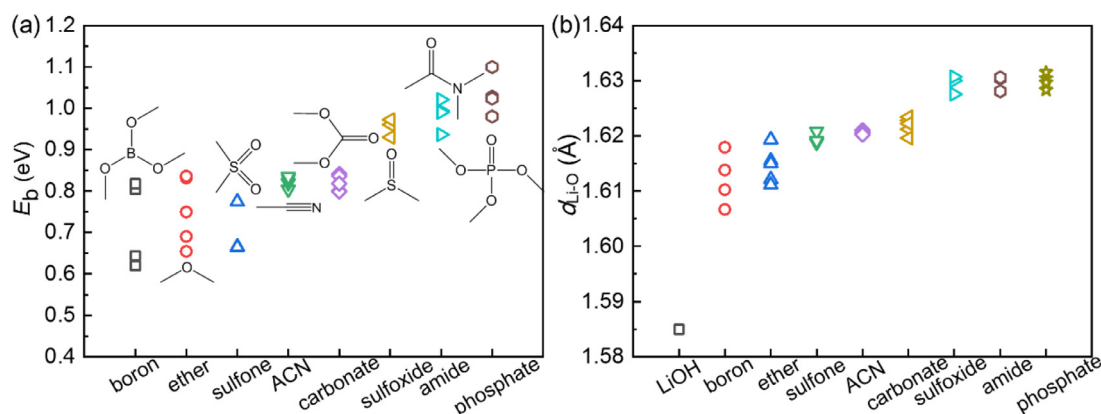


Fig. 5. (a) The binding energy (E_b) of the solvent and LiOH molecule; (b) The Li-O bond length (d_{Li-O}) in LiOH molecule with/without binding to the solvent molecules, the none-bonding LiOH is directly dictated as LiOH, and the LiOH bonding to a solvent molecule is dictated as the solvent types.

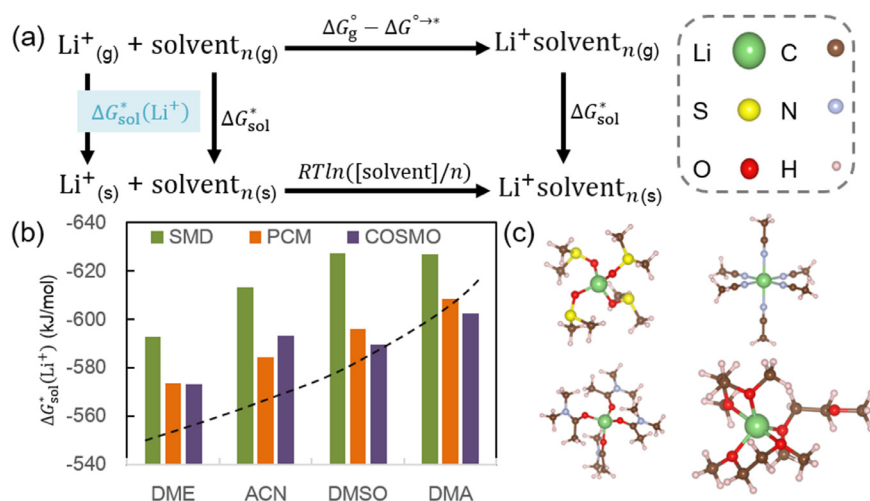


Fig. 6. (a) The cluster thermodynamic cycle for the solvation energy calculation; (b) The solvation energy calculated for different solvents; (c) The optimized cluster structures for Li^+ ions solvated by different solvents, the solvents of which are DMSO (the top left), acetonitrile (ACN, the top right), dimethylacetamide (DMA, the bottom left), dimethoxy ethane (DME, the bottom right), respectively.

Fig. 4b are very simple and are not given here. With these models, the $E_{desorpt}$ and the E_b are calculated and compared as shown in Fig. 4d. It is shown a negative correlation between $E_{desorpt}$ and E_b is observed. In other words, the easier the lithium to detach, the stronger bonding is between the solvent molecule and LiOH. The results suggest the rationality of the model simplification from Fig. 4a to 4b. The nonlinear correlation exists for $E_{desorpt}$ and E_b between the solvents due to the weak interaction in the practical model (Fig. 4c), such as the strong hydrogen bonding interaction between DME and the LiOH surface.

To generalize the solvent effect and thus to facilitate the solvent selection for faster reaction kinetics for the decomposition of LiOH, 33 solvents (Table S5) were collected from the literature and the E_b values (Table S5) were calculated according to the model shown in Fig. 4b. It is noted for those molecules which have different functional groups we only focus on the functional group common in the battery solvent. For example, there are both borate and nitro- group in the nitro-triol borate, we only focus on the borate functional group. Based on the E_b values, the solvent molecules are classified into 8 groups according to the functional groups (Fig. 5a). A result of the solvent-LiOH bond formation is the weakening of the Li-O bond in the LiOH, which is reflected by the bond length of Li-O in LiOH (d_{Li-O}), as shown in Fig. 5b. The variation of d_{Li-O} against the functional group is consistent with E_b as shown in Fig. 5a. It is noted there is overlapping existing in Fig. 5, suggesting the functional group is not sufficient enough to describe the solvent's solvation effect. Based on the analysis of the solvents which have a wide range of E_b , we find that the dipole moment of the solvent also plays a critical role in mediating the E_b . For example, the tetra hydrofuran and

2-emthyl tetra hydrofuran, which have higher dipole moment (~ 1.75 Debye) than that of the other ethers (~ 1.35 Debye) in the ether group, also have higher E_b than that of the other ethers. Fortunately, according to Fig. 5, we can predict that the phosphate-based solvent performs best among the different kinds of solvents investigated.

The final solvation capability of the solvent is indicated as the solvation free energy of the isolated Li^+ ($\Delta G_{sol}^*(Li^+)$) and four common solvents were considered via the cluster thermodynamic cycle (Fig. 6a). The SMD, PCM and COSMO implicit solvation models are considered for comparison.

Fig. 6b and Fig. 6c show the solvation energy for Li^+ in different solvents with different implicit solvation models (SMD, PCM and COSMO) and the solvated structures, respectively. To make the results more persuasive, four typical solvents which are representative in this work and are also precisely described in the solvation models are selected to elucidate the reliability of result predicted from the E_b . It can be seen that the overall trends of the $\Delta G_{sol}^*(Li^+)$ calculated with different implicit solvation models are all consistent with that of the E_b (Fig. 5a), confirming the outperformance of the phosphate-based solvent predicted above. Notably, by comparing the $\Delta G_{sol}^*(Li^+)$ calculated by three different models, we find that although the predictions of the $\Delta G_{sol}^*(Li^+)$ from PCM and COSMO models are a little higher than that from SMD (Fig. 6b), which may be attributed to the different descriptions of the non-electrostatic interaction of these three models, the general trends obtained by these three models are consistent with each other. The consistency between the $E_{desorpt}$, the solvation free energy and the E_b suggests that E_b is a general descriptor to evaluate the solvation capability of the solvent.

The prediction of the solvation effect till now has been focused on the active center as defined in Section S1.5 of the SI, which is usually the oxygen atom in the molecule. However, the similar active centers lead to different solvation capability according to the binding energy and solvation free energy in Fig. 5 and Fig. 6. Thus the local environment around the active center has to play a critical role [35]. To explore the local environment, we resort to the machine learning (ML) [36]. The atom properties (electronegativity) in the functional group and the molecular properties (dipole moment, HOMO and LUMO) are used as features for ML. Three ML models, Gradient Boosting Decision Tree (GBDT), Least Absolute Shrinkage and Selection Operator (LASSO) and Support Vector Regression (SVR), were used to predict the E_b . The results are shown in Fig. S5a. The Fig. S5b shows that the GBDT predicts E_b best among the three models, with a lowest root mean square error (RMSE) of 0.066, as shown in Fig. S5b. To verify the effectiveness of the ML models, we predict the solvent effect (E_b) of five new samples with three models and GBDT obtains a lowest RMSE of 0.045, as shown in Fig. S5c. The results further confirm the reliability of the GBDT model. Therefore, we use GBDT to evaluate the feature importance to further evaluate the solvation effect of different functional groups. It is noted only the features concerning to the atoms in the functional groups are ranked for comparison. As shown in Fig. S5d, the 1_P, representing the phosphate-based functional group, is the most important one, further demonstrating the best performance of the phosphate-based solvent. More details of machine learning details and results can be found in the SI.

It should be noted that although the faster kinetics can be obtained from our simplified model, the practical reaction includes the solid, liquid, and gas phases, all of which may make the gain from the disordered/amorphous structure and solvation effect less dramatic than what predicted in this work. In the future work, more complicated structural and chemical heterogeneity should be considered for a complete description of kinetics at the three-phase interfaces. However, in the meantime, the simplified model presented in this work points to the substantial gains in the performance of RM in Li-air battery.

3. Conclusion

In this work, we establish the correlation of the chemical reaction kinetics between RM and the discharge product structure as well as the solvent via the computational exploration of the OER reaction process. Based on the combination of quantum calculation and machine learning method, we found that (1) the Li^+ desorption is the *rate-determining step* (rds) in the chemical decomposition of the discharge products with the presence of RM in a chemical reaction, (2) the disordered/amorphous discharge product model was first constructed and preferentially to decompose faster compared with the crystalline structure and (3) the phosphate-based solvent is screened out to promote the decomposition kinetics most efficiently among the solvents investigated via its solvation evaluation. The determination of the rds is profound for the kinetics improvement for the OER process. Based on the solvation capability evaluation, the functional group is first demonstrated as the key to effectively describe the solvent's role in regulating the reaction kinetics between RM^+ and the discharge product. Generally, two effective solutions to the sluggish reaction between RM^+ and the discharge product are suggested, i.e., rational disordering design of a discharge product structure and judicious selection of an appropriate solvent. The faster kinetics achievement via the ordering and solvent regulation in this work can also be extended to facilitate the decomposition of other discharge products of the conversion cathodes, such as Li_2O_2 , Li_2CO_3 , sulfides and oxides. Further understanding and improvements can be achieved by taking into account the side reactions, the multi-components of the electrolyte, the complex liquid-solid interface, the non-equilibrium electric potential of the electrode, which entangled together in a cell determine the real reaction and affect the reaction kinetics.

Declaration of Competing Interest

The authors declare no competing financial interest.

CRediT authorship contribution statement

Aiping Wang: Conceptualization, Methodology, Data curation, Writing - original draft. **Zheyi Zou:** Methodology, Validation. **Da Wang:** Supervision, Visualization. **Yue Liu:** Methodology, Software. **Yajie Li:** Writing - review & editing. **Junming Wu:** Methodology, Software. **Maxim Avdeev:** Writing - review & editing. **Siqi Shi:** Conceptualization, Methodology, Validation, Writing - review & editing.

Acknowledgments

We would like to thank Prof. Qing Wang, Zhangquan Peng for fruitful discussions. This work was financially supported by the National Natural Science Foundation of China (Nos. 51802187, 11874254, 51622207, U1630134), Shanghai Sailing Program (No. 18YF1408700), Shanghai Pujiang Program (No. 2019PJJD016), Open Project of the State Key Laboratory of Advanced Special Steel, Shanghai University, China (No. SKLASS2018-01), the Project of the State Key Laboratory of Advanced Special Steel, Shanghai University, China (No. SKLASS2019-Z023) and the Science and Technology Commission of Shanghai Municipality (No. 19DZ2270200). We appreciate the High Performance Computing Center of Shanghai University, and Shanghai Engineering Research Center of Intelligent Computing System (No. 19DZ2252600) for providing the computing resources and technical support.

Supplementary materials

Supplementary material associated with this article can be found, in the online version, at doi:[10.1016/j.ensm.2020.10.022](https://doi.org/10.1016/j.ensm.2020.10.022).

References

- [1] J. Lu, L. Li, J.B. Park, Y.K. Sun, F. Wu, K. Amine, Aprotic and Aqueous Li-O Batteries, *Chem. Rev.* 114 (2014) 5611–5640, doi:[10.1021/cr400573b](https://doi.org/10.1021/cr400573b).
- [2] G.V. Chase, S. Zecevic, W.T. Wesley, J. Uddin, K.A. Sasaki, G.P. Vincent, V. Bryantsev, M. Blanco, D.D. Addison, Soluble Oxygen Evolving Catalysts for Rechargeable Metal-air Batteries, US, 2012.
- [3] Y. Chen, S.A. Freunberger, Z. Peng, O. Fontaine, P.G. Bruce, Charging a Li-O₂ battery using a redox mediator, *Nat. Chem.* 5 (2013) 489–494, doi:[10.1038/nchem.1646](https://doi.org/10.1038/nchem.1646).
- [4] J. Zhang, B. Sun, X. Xie, Y. Zhao, G. Wang, A Bifunctional Organic Redox Catalyst for Rechargeable Lithium–Oxygen Batteries with Enhanced Performances, *Adv. Sci.* 3 (2016) 1500285, doi:[10.1002/adv.201500285](https://doi.org/10.1002/adv.201500285).
- [5] H.-D. Lim, B. Lee, Y. Zheng, J. Hong, J. Kim, H. Gwon, Y. Ko, M. Lee, K. Cho, K. Kang, Rational design of redox mediators for advanced Li-O₂ batteries, *Nat. Energy* 1 (2016) 16066, doi:[10.1038/nenergy.2016.66](https://doi.org/10.1038/nenergy.2016.66).
- [6] Y. Chen, X. Gao, L.R. Johnson, P.G. Bruce, Kinetics of Lithium Peroxide Oxidation by Redox Mediators and Consequences for the Lithium–Oxygen Cell, *Nat. Commun.* 9 (2018) 767, doi:[10.1038/s41467-018-03204-0](https://doi.org/10.1038/s41467-018-03204-0).
- [7] S. Wu, Y. Qiao, H. Deng, Y. He, H. Zhou, Minimizing the Abnormal High-Potential Discharge Process Related to Redox Mediators in Lithium–Oxygen Batteries, *J. Phys. Chem. Lett.* 9 (2018) 6761–6766, doi:[10.1021/acs.jpclett.8b02899](https://doi.org/10.1021/acs.jpclett.8b02899).
- [8] Y.G. Zhu, C. Jia, J. Yang, F. Pan, Q. Huang, Q. Wang, Dual redox catalysts for oxygen reduction and evolution reactions: towards a redox flow Li-O₂ battery, *Chem. Commun.* 51 (2015) 9451–9454, doi:[10.1039/c5cc01616a](https://doi.org/10.1039/c5cc01616a).
- [9] T. Zhang, K. Liao, P. He, H. Zhou, A self-defense redox mediator for efficient lithium-O₂ batteries, *Energy Environ. Sci.* 9 (2016) 1024–1030, doi:[10.1039/c5ee02803e](https://doi.org/10.1039/c5ee02803e).
- [10] Z. Guo, C. Li, J. Liu, Y. Wang, Y. Xia, A Long-Life Lithium-Air Battery in Ambient Air with a Polymer Electrolyte Containing a Redox Mediator, *Angew. Chem. Int. Ed.* 56 (2017) 7505–7509, doi:[10.1002/anie.201701290](https://doi.org/10.1002/anie.201701290).
- [11] Y. Ko, H. Park, B. Lee, Y. Bae, S.K. Park, K. Kang, A comparative kinetic study of redox mediators for high-power lithium–oxygen batteries, *J. Mater. Chem. A* 7 (2019) 6491–6498, doi:[10.1039/C9TA00096H](https://doi.org/10.1039/C9TA00096H).
- [12] J.S. Hummelshøj, A.C. Luntz, J.K. Nørskov, Theoretical evidence for low kinetic overpotentials in Li-O₂ electrochemistry, *J. Chem. Phys.* 138 (2013) 034703, doi:[10.1063/1.4773242](https://doi.org/10.1063/1.4773242).
- [13] C. Ling, R. Zhang, K. Takechi, F. Mizuno, Intrinsic Barrier to Electrochemically Decompose LiCO and LiOH, *J. Phys. Chem. C* 118 (2014) 26591–26598, doi:[10.1021/jp5093306](https://doi.org/10.1021/jp5093306).
- [14] W. Zhang, Y. Shen, D. Sun, Z. Huang, J. Zhou, H. Yan, Y. Huang, Promoting Li₂O₂ oxidation via solvent-assisted redox shuttle process for low overpotential Li-O₂ battery, *Nano Energy* 30 (2016) 43–51, doi:[10.1016/j.nanoen.2016.09.031](https://doi.org/10.1016/j.nanoen.2016.09.031).

- [15] Y. Sun, H. Zhou, Facilitating the Oxygen Evolution Reaction of Lithium Peroxide via Molecular Adsorption, *J. Phys. Chem. C* 120 (2016) 10237–10243, doi:[10.1021/acs.jpcc.6b00413](https://doi.org/10.1021/acs.jpcc.6b00413).
- [16] Z. Li, S. Ganapathy, Y. Xu, J.R. Heringa, Q. Zhu, W. Chen, M. Wagemaker, Understanding the Electrochemical Formation and Decomposition of Li_2O_2 and LiOH with Operando X-ray Diffraction, *Chem. Mater.* 29 (2017) 1577–1586, doi:[10.1021/acs.chemmater.6b04370](https://doi.org/10.1021/acs.chemmater.6b04370).
- [17] D.G. Kwabi, V.S. Bryantsev, T.P. Batcho, D.M. Itkis, C.V. Thompson, Y. Shao-Horn, Experimental and Computational Analysis of the Solvent-Dependent $\text{O}_2/\text{Li}^+-\text{O}_2^-$ Redox Couple: Standard Potentials, Coupling Strength, and Implications for Lithium-Oxygen Batteries, *Angew. Chem. Int. Ed.* 55 (2016) 3129–3134, doi:[10.1002/anie.201509143](https://doi.org/10.1002/anie.201509143).
- [18] T. Liu, M. Leskes, W. Yu, A.J. Moore, L. Zhou, P.M. Bayley, G. Kim, C.P. Grey, Cycling $\text{Li}-\text{O}_2$ batteries via LiOH formation and decomposition, *Science* 350 (2015) 530–533, doi:[10.1126/science.aac7730](https://doi.org/10.1126/science.aac7730).
- [19] Y. Qiao, S. Wu, J. Yi, Y. Sun, S. Guo, S. Yang, P. He, H. Zhou, From O_2^- to HO_2^- : Reducing By-Products and Overpotential in $\text{Li}-\text{O}_2$ Batteries by Water Addition, *Angew. Chem. Int. Ed.* 56 (2017) 4960–4964, doi:[10.1002/anie.201611122](https://doi.org/10.1002/anie.201611122).
- [20] Y.G. Zhu, Q. Liu, Y. Rong, H. Chen, J. Yang, C. Jia, L.J. Yu, A. Karton, Y. Ren, X. Xu, S. Adams, Q. Wang, Proton enhanced dynamic battery chemistry for aprotic lithium-oxygen batteries, *Nat. Commun.* 8 (2017) 14308, doi:[10.1038/ncomms14308](https://doi.org/10.1038/ncomms14308).
- [21] M. Tulodziecki, G.M. Leverick, C.V. Amannchukwu, Y. Katayama, D.G. Kwabi, F. Barde, P.T. Hammond, Y. Shao-Horn, The role of iodide in the formation of lithium hydroxide in lithium-oxygen batteries, *Energy Environ. Sci.* 10 (2017) 1828–1842, doi:[10.1039/c7ee00954b](https://doi.org/10.1039/c7ee00954b).
- [22] T. Liu, G. Kim, E. Jónsson, E. Castillo-Martinez, I. Temprano, Y. Shao, J. Carretero-González, R.N. Kerber, C.P. Grey, Understanding LiOH Formation in a $\text{Li}-\text{O}_2$ Battery with LiI and H_2O Additives, *ACS Catal.* 9 (2018) 66–77, doi:[10.1021/acscatal.8b02783](https://doi.org/10.1021/acscatal.8b02783).
- [23] Y. Qiao, S. Wu, Y. Sun, S. Guo, J. Yi, P. He, H. Zhou, Unraveling the Complex Role of Iodide Additives in $\text{Li}-\text{O}_2$ Batteries, *ACS Energy Lett.* 2 (2017) 1869–1878, doi:[10.1021/acsenenergylett.7b00462](https://doi.org/10.1021/acsenenergylett.7b00462).
- [24] X. Zeng, L. Leng, F. Liu, G. Wang, Y. Dong, L. Du, L. Liu, S. Liao, Enhanced $\text{Li}-\text{O}_2$ battery performance, using graphene-like nori-derived carbon as the cathode and adding LiI in the electrolyte as a promoter, *Electrochim. Acta* 200 (2016) 231–238, doi:[10.1016/j.electacta.2016.03.161](https://doi.org/10.1016/j.electacta.2016.03.161).
- [25] S. Shi, J. Gao, Y. Liu, Y. Zhao, Q. Wu, W. Ju, C. Ouyang, R. Xiao, Multi-scale computation methods: Their applications in lithium-ion battery research and development, *Chin. Phys. B* 25 (2016) 018212, doi:[10.1088/1674-1056/25/1/018212](https://doi.org/10.1088/1674-1056/25/1/018212).
- [26] F. Li, S. Wu, D. Li, T. Zhang, P. He, A. Yamada, H. Zhou, The water catalysis at oxygen cathodes of lithium-oxygen cells, *Nat. Commun.* 6 (2015) 7843, doi:[10.1038/ncomms8843](https://doi.org/10.1038/ncomms8843).
- [27] M. Bonomo, A. Carella, F. Borbone, L. Rosato, D. Dini, L. Gontrani, New pyran-based molecules as both n- and p-type sensitizers in semi-transparent Dye Sensitized Solar Cells, *Dyes Pigm.* 175 (2020) 108140, doi:[10.1016/j.dyepig.2019.108140](https://doi.org/10.1016/j.dyepig.2019.108140).
- [28] P. Ravindran, R. Asokamani, Correlation between Electronic Structure, Mechanical Properties and Phase Stability in Intermetallic Compounds, *Bull. Mater. Sci.* 20 (1997) 613–622, doi:[10.1007/BF02744780](https://doi.org/10.1007/BF02744780).
- [29] W. Zhao, P.H. Tan, J. Liu, A.C. Ferrari, Intercalation of Few-Layer Graphite Flakes with FeCl_3 : Raman Determination of Fermi Level, Layer by Layer Decoupling, and Stability, *J. Am. Chem. Soc.* 133 (2011) 5941–5946, doi:[10.1021/ja110939a](https://doi.org/10.1021/ja110939a).
- [30] W.-J. Kwak, D. Hirshberg, D. Sharon, M. Afri, A.A. Frimer, H.-G. Jung, D. Aurbach, Y.-K. Sun, $\text{Li}-\text{O}_2$ cells with LiBr as an electrolyte and a redox mediator, *Energy Environ. Sci.* 9 (2016) 2334–2345, doi:[10.1039/c6ee00700g](https://doi.org/10.1039/c6ee00700g).
- [31] X.-G. Wang, C. Wang, Z. Xie, X. Zhang, Y. Chen, D. Wu, Z. Zhou, Improving Electrochemical Performances of Rechargeable $\text{Li}-\text{CO}_2$ Batteries with an Electrolyte Redox Mediator, *ChemElectroChem* 4 (2017) 2145–2149, doi:[10.1002/celec.201700539](https://doi.org/10.1002/celec.201700539).
- [32] Y. Hou, J. Wang, L. Liu, Y. Liu, S. Chou, D. Shi, H. Liu, Y. Wu, W. Zhang, J. Chen, MoC/CNT : An Efficient Catalyst for Rechargeable $\text{Li}-\text{CO}_2$ Batteries, *Adv. Funct. Mater.* 27 (2017) 1700564, doi:[10.1002/adfm.201700564](https://doi.org/10.1002/adfm.201700564).
- [33] S. Sankarasubramanian, J. Kahky, V. Ramani, Tuning anion solvation energetics enhances potassium-oxygen battery performance, *Proc. Natl. Acad. Sci.* 116 (2019) 14899–14904, doi:[10.1073/pnas.1901329116](https://doi.org/10.1073/pnas.1901329116).
- [34] M. Okoshi, Y. Yamada, A. Yamada, H. Nakai, Theoretical Analysis on De-Solvation of Lithium, Sodium, and Magnesium Cations to Organic Electrolyte Solvents, *J. Electrochem. Soc.* 160 (2013) A2160–A2165, doi:[10.1149/2.074311jes](https://doi.org/10.1149/2.074311jes).
- [35] H. Xu, D. Cheng, D. Cao, X.C. Zeng, A universal principle for a rational design of single-atom electrocatalysts, *Nat. Catal.* 1 (2018) 339–348, doi:[10.1038/s41929-018-0063-z](https://doi.org/10.1038/s41929-018-0063-z).
- [36] Y. Liu, B. Guo, X. Zou, Y. Li, S. Shi, Machine learning assisted materials design and discovery for rechargeable batteries, *Energy Storage Mater.* 31 (2020) 434–450 <https://doi.org/10.1016/j.ensm.2020.06.033>.

Supplementary Information for

Identifying Chemical Factors Affecting Reaction Kinetics in Li-air Battery via *ab initio* Calculations and Machine Learning

Aiping Wang ^a, Zheyi Zou ^a, Da Wang ^a, Yue Liu ^b, Yajie Li ^a, Junming Wu ^b, Maxim Avdeev ^{c,d}, Siqi Shi ^{a,e,*}

^a *State Key Laboratory of Advanced Special Steel, Shanghai Key Laboratory of Advanced Ferrometallurgy, School of Materials Science and Engineering, Shanghai University, Shanghai 200444, China*

^b *School of Computer Engineering and Science, Shanghai Institute for Advanced Communication and Data Science, Shanghai University, Shanghai 200444, China*

^c *Australian Nuclear Science and Technology Organisation, Locked Bag 2001, Kirrawee DC NSW 2232, Australia*

^d *School of Chemistry, The University of Sydney, Sydney 2006, Australia*

^e *Materials Genome Institute, Shanghai University, Shanghai 200444, China*

*Email: sqshi@shu.edu.cn (Siqi Shi)

Contents

S1. Methods and Details.....	2
S1.1. Calculation Details and Model Construction	2
S1.2. Redox Potential Calculation.....	5
S1.3. Reaction Path Anatomy	5
S1.4. Amorphous Model Construction for Li ₂ CO ₃	8
S1.5. Definition of the Active Center	8
S1.6. Thermodynamics of the Self-solvation	8
S1.7. Model Validation for the Simplification	10
S1.8. Machine Learning Method to Predict the Solvent Effect	10
S2. Figures.....	12
S3. Tables.....	19
References.....	35

S1 Methods and Details

S1.1 Calculation Details and Model Construction

The OER process of Li-air battery with RM involved includes two steps, *i.e.*, the electrochemical step and the chemical step. The electrochemical part was conducted using the Gaussian 09.[1] For the iodine species, geometries were optimized at the M06-L/Stuttgart RLC ECP level.[2, 3] The single point energies were calculated at the M05-2X/Stuttgart RLC ECP level including the implicit solvation energy described by SMD[4] model.

The chemical reaction process calculation were performed with the Vienna Ab-initio Simulation Package (VASP),[5-8] where the projector plane wave (PAW) approach was employed to describe the core-valance electron interactions.[9, 10] The Perdew-Burke-Ernzerhof (PBE) generalized gradient approximation (GGA)[11] was used to describe the electron interactions, where the number of plane waves is determined by the cut-off energy (E_{cut}) consistent in all systems. Spin-polarization and vdW corrections[12] were implemented in all calculations. A *cut-off* for the plane wave basis was set to 400 eV coupled with the Γ -point centered scheme for *k-point* sampling. A Gaussian smearing of 0.05 eV was used for Fermi – Dirac distribution. A non-symmetric slab model was used for the reaction process calculations. The dipole correction was tested and found negligible in the reaction investigation.[13, 14] The electronic structure was relaxed to an energy tolerance of 10^{-4} eV and the geometry was optimized to a force tolerance within 0.03 eV/Å. For surface calculations, the cell

containing a slab of 162 atoms for LiOH was used, and a vacuum layer of 20 Å was set. The *k-point* meshes were sampled as 1×1×1 other than the electronic structure calculation, for which a 3×3×1 mesh and a *cut-off* of 500 eV were used. The core electron level of oxygen was aligned as the reference energy level for electronic structure analysis. For the molecule/cluster calculation, the cell was set as 20×20×20 Å³.

Furthermore, the solvent property and the solvent effect involving the solvation of cation Li⁺ was also calculated with the Gaussian 09,[1] The solvent effect used the mixed cluster/continuum model via a thermodynamic cycle. Three implicit solvation models, SMD,[4] PCM[15] and COMSO,[16, 17] were used. The geometries optimization and thermal correction were calculated at the B3LYP/6-31g* level. The Highest Unoccupied Molecular Orbital (HOMO), Lowest Unoccupied Molecular Orbital (LUMO), and dipole moment (μ) were obtained at the B3LYP/6-311g* level. The single point energies were obtained at the B3LYP/6-311++g** level and the solvation free energy calculation for SMD was calculated at the M05-2X/6-31g* level and for the other two models was calculated at the HF/6-31g* level.

To further consider the influence of the local environment (in contrast to the active center) of the solvent molecule on the solvent effect, the Machine Learning method was used. The gradient boosting decision tree (GBDT)[18-20] method was used to predict the E_b (the binding energy between LiOH and the solvent molecule) by only considering the nearest coordinated and the second nearest coordinated atom type

(electronegativity) as well as the coordination number. The feature importance was further ranked by the GBDT method as detailed in the SI.

The disordered/amorphous structure model of LiOH was constructed within the Amorphous Cell[21-23], which maintains the chemical properties of the compound. The candidate units are placed into a three-dimensional box via growing, *i.e.*, each unit is placed one by one, taking into account the interaction. The next candidate to be chosen is with judicious consideration by comparing the probability based on the energy of different candidate unit placement. An initial density of 1.46 g/cm³ was used, with reference to the crystalline structure. The initial disordered/amorphous model was double optimized within VASP suite using the input parameters mentioned above. To confirm the reasonableness of our disordered/amorphous model, the amorphous Li₂CO₃ was also constructed using the same method and the radial distribution functions (Fig. S8) are consistent with that constructed from the commonly used molecular dynamics (MD) manner,[24] as detailed in the SI.

Additionally, the DFT behaves poorly in describing the triplet state of O₂ by overestimating the binding energy.[25] To eliminate the error, the enthalpy of O₂ was calculated with the O atom enthalpy and the experimental binding energy ($\Delta E^{\text{exptl}} = 5.12 \text{ eV}$)[26] as:

$$H(\text{O}_2, 0 \text{ K}) = 2H(\text{O}, 0 \text{ K}) - \Delta E^{\text{exptl}}$$

where $H(\text{O}, 0 \text{ K})$ is the calculated ground-state enthalpy of an oxygen atom. All the other reference species concerning to the reaction process, such as LiI and OH for path

1, LiI, H₂O for path 2, and H₂O₂ and LiI for path 3, were obtained in the vacuum at 0 K.

S1.2 Redox Potential Calculation

The redox potential was calculated according to the ideal chemical and electrochemical energy conversion formula as:

$$\Delta G = -nFE_{abs} \quad (S1)$$

where ΔG is the Gibbs free energy difference of the electrochemical reaction, n is the number of electron transfer, F is the Faraday constant and E_{abs} is the absolute redox potential. The thermodynamic cycle method[27, 28], as illustrated in Fig. S9, has been used to calculate the reaction Gibbs free energy, ΔG , as:

$$\Delta G = -\Delta G_{sol}(A) + \Delta G_g + \Delta G_{sol}(A^+) + \Sigma \Delta G^{o \rightarrow *} \quad (S2)$$

where, A and A^+ are the reduction and oxidation state, respectively; $\Sigma \Delta G^{o \rightarrow *}$ is the conversion free energy from an ideal gas at a concentration of 1 atm to an ideal gas at a concentration of 1 mol/L.[29] The other description code can be referred to from the caption of Fig. S9. Adiabatic absolute redox potential was calculated in this work, where the adiabatic potential suggests both the reactant and the product are in the optimized state. The electron energy is set to 0, thus the redox potential calculated by Equation (Eq.) S1 is relative to the energy level of the electron at rest in vacuum. The redox potential vs. Li/Li⁺ in Table 1 was converted by subtracting 1.4 V.[30]

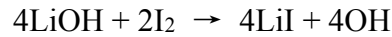
S1.3 Reaction Path Anatomy

The corresponding reaction steps of the three paths investigated are listed, among which path 1 is adopted from the work of Ling *et al.*[31] by introducing the iodine. The reaction energy of each path performed on (001) and (100) surfaces are given in Table

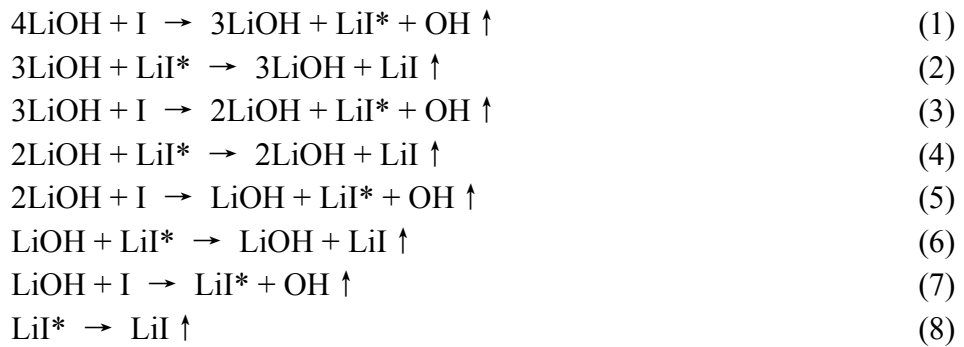
S2. The reaction path presentation is separated into two parts, the overall reaction and the disassembled reaction of each reaction step, which are presented as reaction equations. It is noted that the formation of the adsorbed species is denoted with a star (*) and desorption is denoted with an upward arrow (↑). The reaction equations of each path are ordered independent from other equations.

The reaction process of path 1 is comprehensively described as: (1) the LiI forms and the OH group desorbs; (2) the LiI desorbs; (3) the LiI forms and the OH group desorbs; (4) the LiI desorbs; (5) the LiI forms and the OH group desorbs; (6) the LiI desorbs; (7) the LiI forms and the OH group desorbs; (8) the LiI desorbs.

Overall reaction of path 1[31]:

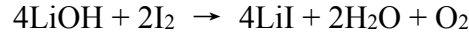


Disassembled reaction equations of path 1:

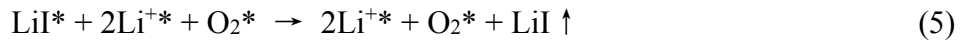
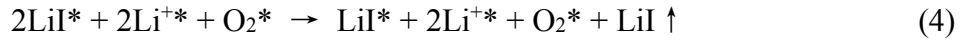
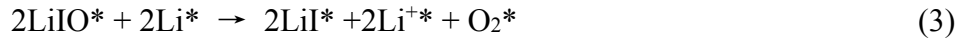
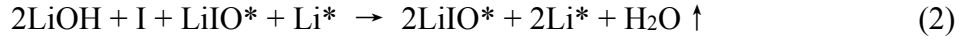
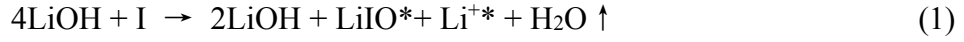


The reaction process of path 2 is comprehensively described as: (1) the H₂O forms and desorbs; (2) the H₂O forms and desorbs; (3) the O₂ forms; (4) the first LiI desorbs; (5) the LiI desorbs; (6) the O₂ desorbs; (7) the third LiI desorbs; (8) the LiI desorbs.

Overall reaction of path 2:



Disassembled reaction equations of path 2:

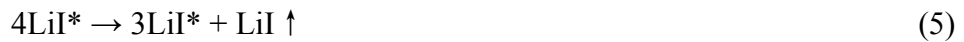
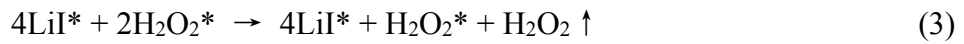
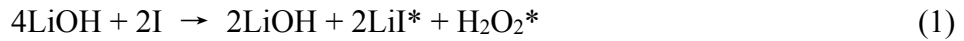


The reaction process of path 3 is comprehensively described as: (1) the H_2O_2 forms; (2) the H_2O_2 forms; (3) one H_2O_2 desorbs; (4) the other H_2O_2 desorbs; (5) the LiI desorbs; (6) the LiI desorbs; (7) the LiI desorbs; (8) the LiI desorbs. In contrast to path 2, path 3 considers the formation of H_2O_2 rather than H_2O .

Overall reaction of path 3:



Reaction coordinates of path 3:



S1.4 Amorphous Model Construction for Li_2CO_3

As the ionic compound is separated into the cation and the anion rather than single atoms to maintain the chemical property of a material, Li_2CO_3 is separated into two Li and one CO_3 molecule. The density is set to 2.096 g/cm^3 , similar to the crystalline one. For a system containing 20 formula of Li_2CO_3 , there are 40 Li and 20 CO_3 molecule, which were packed into a cubic cell of $10.539 \times 10.539 \times 10.539 \text{ \AA}^3$. The radial distribution functions were shown in Fig. S8, consistent with the commonly used method in constructing the amorphous model.[24] Usually, the amorphous model construction is started from a crystalline one and heated to a temperature above the melting point, obtaining the liquid phase. Then, the liquid phase is quenched with an extremely fast rate (around 10^{12} K/s or even higher) to generate the amorphous phase.

S1.5 Definition of the Active Center

The atom akin to bind to the lithium is defined as the active center of the solvent molecule. The largest electronegativity difference (ΔEN) rule is proposed, defined as the electronegativity difference between the lithium and the atom in the solvent molecule. The electronegativity referred are listed in Table S6. With DMSO as an example, all types of the atoms in DMSO have been tested by calculating the E_b . The schematics of the models and the results are shown in Table S7, suggesting that the higher the electronegativity, the higher the E_b will be, verifying the largest ΔEN rule.

S1.6 Thermodynamics of the Self-solvation

The chemical potential of a solute X in the ideal gas state and the infinite dilute

solution state under a certain condition (T, P) can be stated as

$$\mu_g(X) = \mu_g^\infty(X) + RT \ln[X_g] \quad (S3)$$

$$\begin{aligned} \mu_{\text{solv}}(X) &= \mu_{\text{solv}}^\infty(X) + RT \ln[X_{\text{solv}}] \\ &= \mu_g^\infty(X) + N_A W(X|\text{solvent}) + RT \ln[X_{\text{solv}}] \end{aligned} \quad (S4)$$

Where R is the universal gas constant, N_A is the Avogadro's number, $[X_g]$ and $[X_{\text{solv}}]$ are the molarities. $^\infty$ means the standard state of 1 M for the hypothetical ideal gas and the hypothetical infinite dilute solution.

The solvation free energy of a solute is defined as the Gibbs free energy transfer of one mole solute from the ideal gas state to the infinite dilute solution state, i.e., the chemical potential difference between the two states. Thus, the solvation free energy of a solute is:

$$\Delta G_{\text{solv}}^* = \mu_{\text{solv}}(X) - \mu_g(X) \quad (S5)$$

Substituting Eq. S3 and S4 into Eq. S5 yields

$$\Delta G_{\text{solv}}^*(X) = N_A W(X|\text{solvent}) \quad (S6)$$

When considering the self-solvation free energy, from the equilibrium between the solvent and its gas, it yields

$$\mu_{\text{solv}}(X) = \mu_g(X) \quad (S7)$$

Thus, we can have

$$\Delta G_{\text{self}}^* = \Delta G_{\text{solv}}^*(X) = RT \ln \left(\frac{[X_g]}{[X_{\text{solv}}]} \right) \quad (S8)$$

Where the $[X_g]$ and $[X_{\text{solv}}]$ are the saturation vapor and liquid molarities.

Substituting the saturation vapor[32] $[X_g]$ and liquid molarities $[X_{\text{solv}}]$ of the solvent into Eq. S8, we got the derived experimental values, as shown in Table S5,

noted as the experimental values.

S1.7 Model Validation for the Simplification

The model transforms from Fig. 4a to Fig. 4b can be rationalized by the lithium desorption energy (E_{desorpt}). Three common solvents were accounted, DME, ACN and DMSO (Fig. 4d). The calculated E_{desorpt} is shown in Table S8. It can be found that the variation of the E_{desorpt} for different solvent is consistent with the E_b variation, suggesting the rationality of the model simplification.

S1.8 Machine Learning Method to Predict the Solvent Effect

There are 33 solvent molecules involved, as schematically shown in Table S4. The features include the molecule property, the Highest Unoccupied Molecular Orbital (HOMO), Lowest Unoccupied Molecular Orbital (LUMO), and dipole moment (μ), and the atom property of the functional group. The latter is formatted as site_atom, where the site is the atom site, dictated with three numbers, 0, 1, 2, representing the active center, the nearest coordinate site of the active center, the second nearest coordinate site of the active center, respectively. The value of site_atom is the electronegativity of the atom at the site multiplies the number of it. The details are presented in Table S9.

Three machine learning (ML) models, the Gradient Boosting Decision Tree (GBDT)[18-20], Least Absolute Shrinkage and Selection Operator (LASSO)[33] and Support Vector Regression (SVR)[34], have been chosen as they perform well for predicting the small sample size.[35-37] Among the three models, the GBDT and the

LASSO can also give the feature importance, which can help us to understand the samples deeply. The “Leave-One-Out” cross validation method was used to train and determine the best ML model. The grid search optimization was used to determine the hyperparameter. Firstly, we used the first 28 samples in Table S9 to train the ML models. Then, to verify the effectiveness of these models, we used them to predict the E_b of 5 new samples (the last five samples in Table S9) which have not been involved to train the model. Lastly, the feature importance concerning to the functional group was evaluated with the GBDT model.

S2 Figures

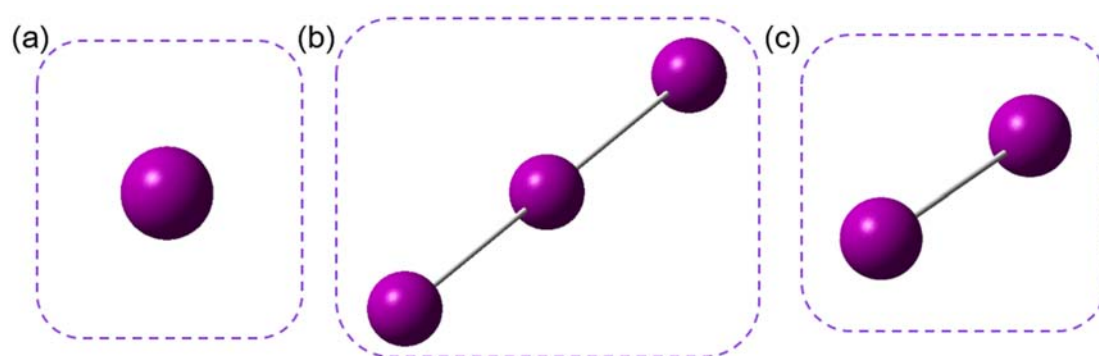


Fig. S1. Optimized geometries of iodine species: (a) I; (b) I_3^- ; (c) I_2 . Linear I_3^- was considered in this work due to its higher stability compared with that of the non-linear one.

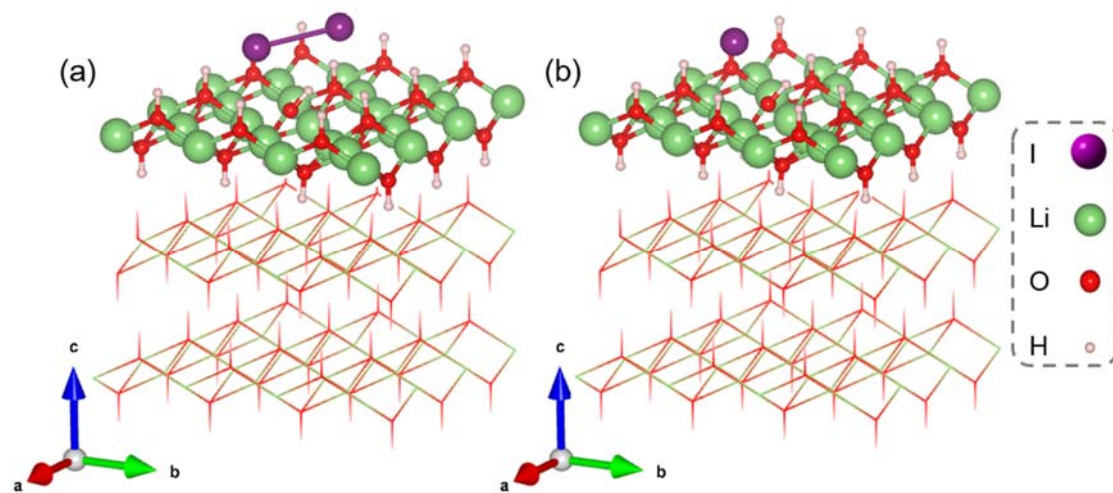


Fig. S2. Geometries for the adsorbed (a) I₂* and (b) I* on the (001) surface, respectively.

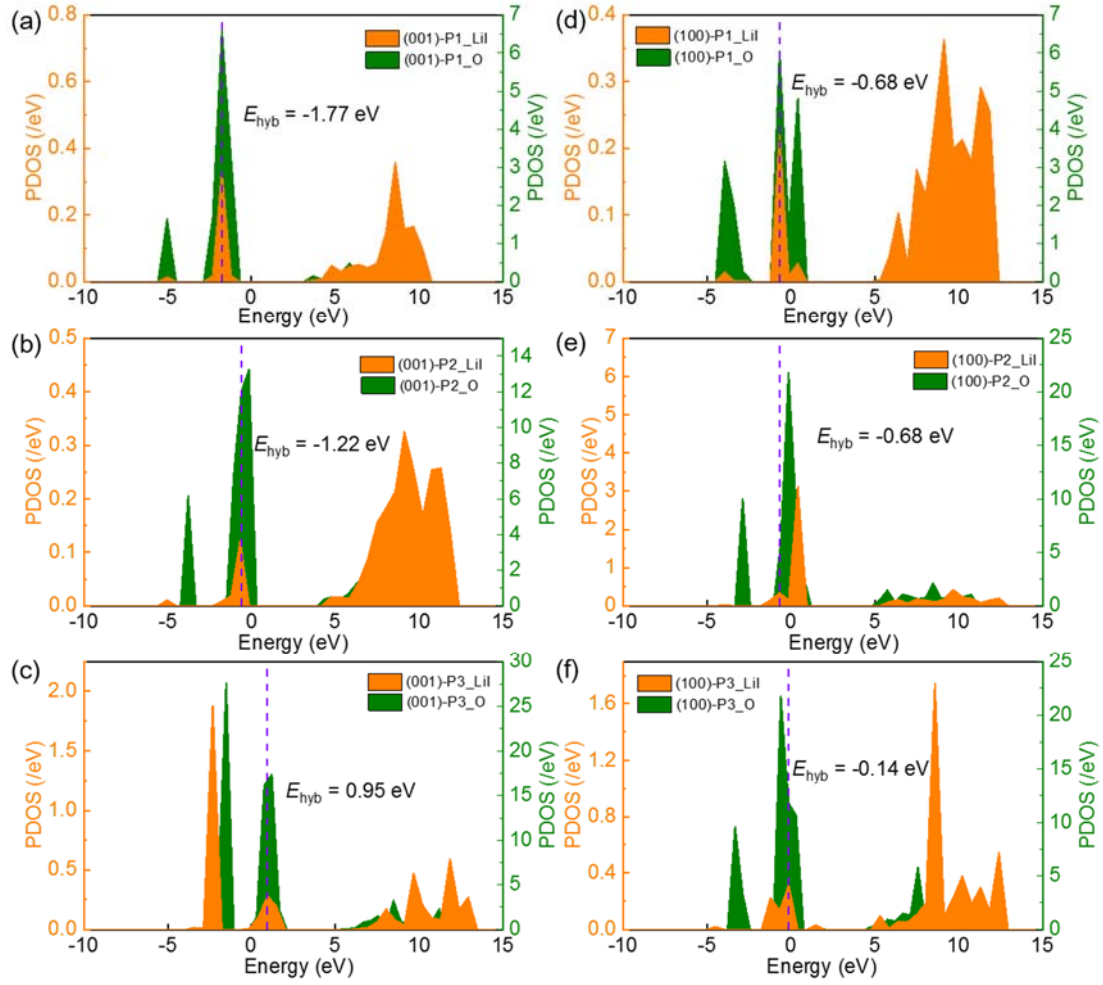


Fig. S3. (a), (b), (c) and (d), (e), (f) are the projected density of states (PDOS) of the structure prior the *rd*s reaction for different paths performed in the (001) and (100) surfaces, respectively. The hybridization energy level (E_{hyb} , denoted with the dashed purple line) between the LiI which is about to desorb and the oxygen of the matrix has been aligned according to the 2s orbital of the oxygen in the system.

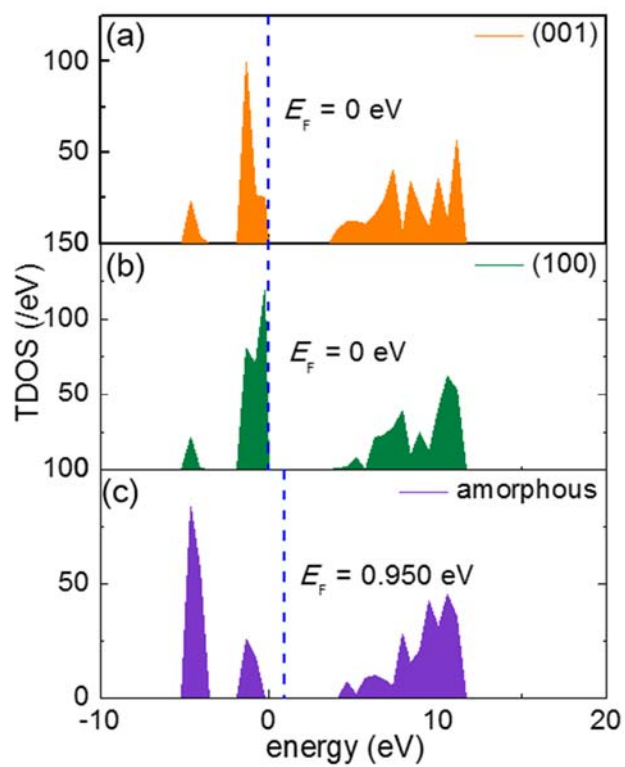


Fig. S4. The total density of states (TDOS) for (a) (001), (b) (100) and (c) amorphous surface model, only the spin up DOS was plotted. The Fermi level (E_F) is noted as the dashed blue line.

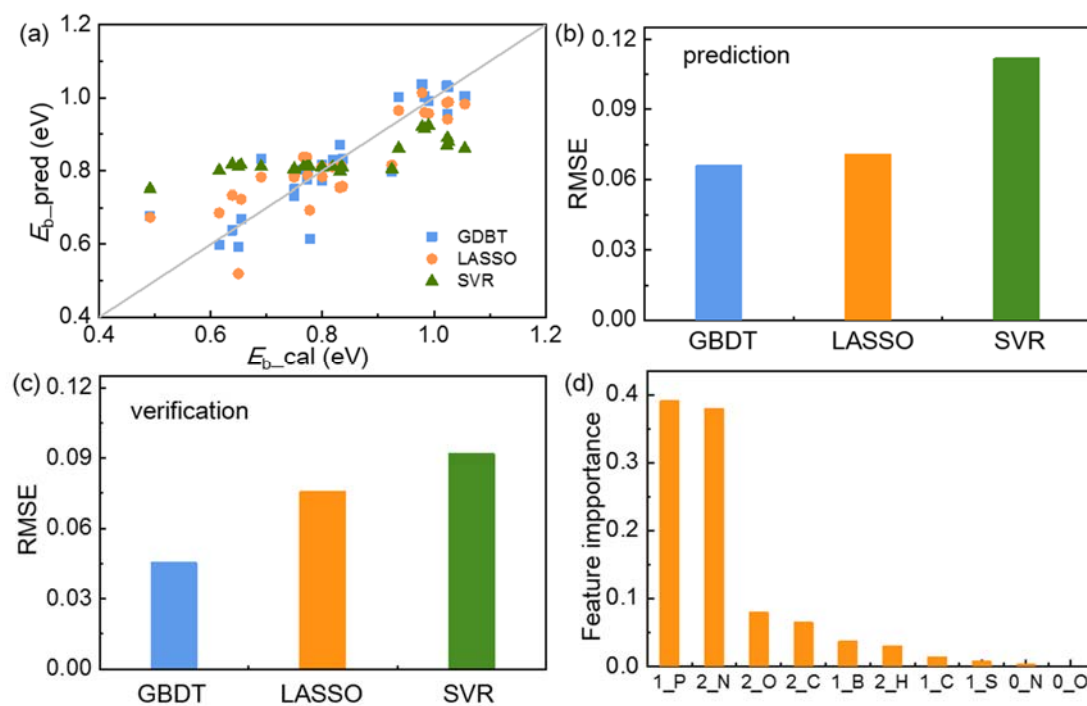


Fig. S5. (a) The predicted E_{b_pred} with different ML models are plotted against the calculated E_{b_cal} for the solvents in the training set, (b) and (c) are the RMSEs of the models in the prediction and verification process, (d) is the feature importance ranking for different features concerning to the functional group.

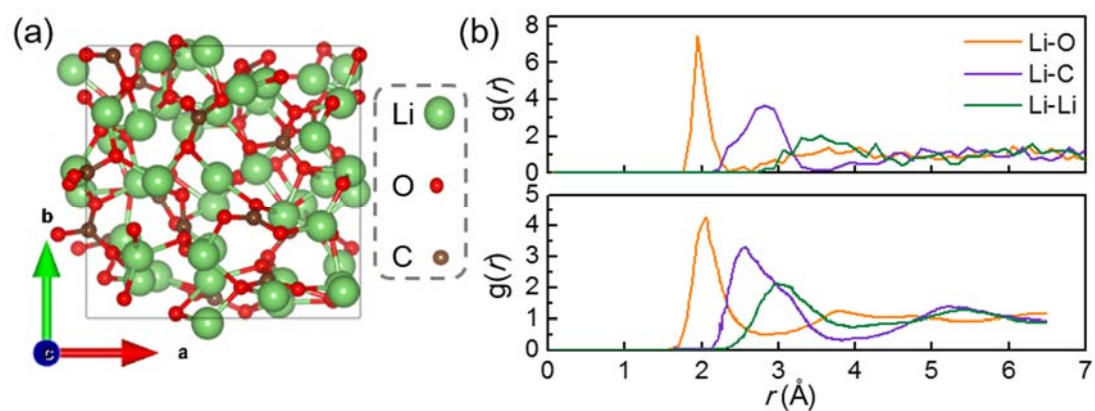


Fig. S6. (a) Amorphous structure and (b) radial distribution functions (RDF) for Li_2CO_3 . The up-panel of (b) is the RDF amorphous model of Li_2CO_3 constructed using our method and the down-panel of (b) is the RDF for the amorphous Li_2CO_3 using the molecular dynamics, adapted from Ref[24]. (Copyright: 1996-2019 MDPI (Basel, Switzerland))

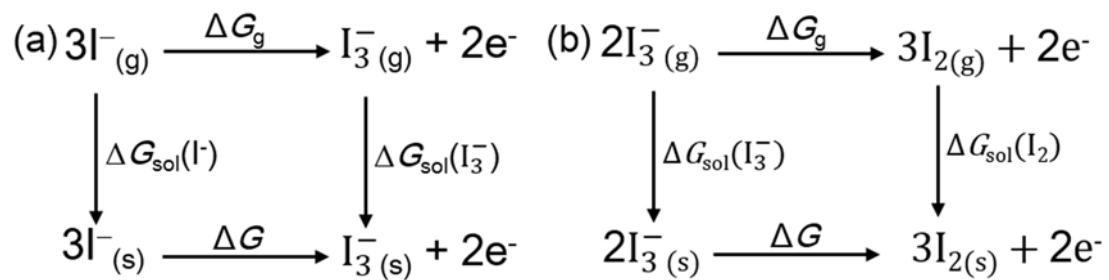


Fig. S7. Thermodynamic cycles for calculating the electrochemical reaction energy, (a) I^-/I_3^- ; (b) I_3^-/I_2 . Subscripts _g and _s indicate the gas and solution state; ΔG_{g} is the reaction Gibbs free energy in the gas state; ΔG_{sol} is the solvation free energy.

S3 Tables

Table S1 The redox potentials calculated by the direct method and obtained from the experiments are listed.

Redox couple	Redox potential vs. Li/Li ⁺ (V)		
	Direct calculation[38] ^a	Expt.[39]	Expt.[40]
I ⁻ /I ₃ ⁻	3.49	3.2	3.28
I ₃ ⁻ /I ₂	4.12	3.7	3.60

^a The optimizations of all geometries were conducted at M06-L/Stuttgart level and the solvation energy calculations were conducted at the M05-2X/Stuttgart level.

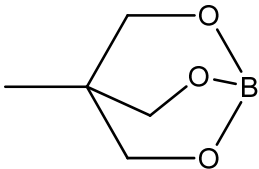
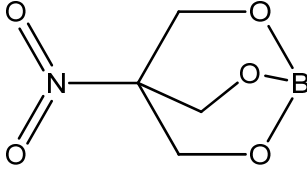
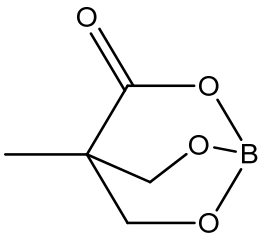
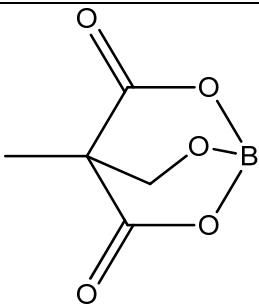
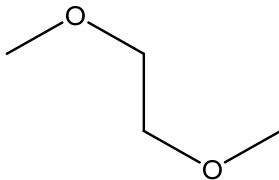
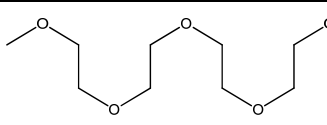
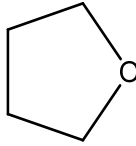
Table S2. The relative reaction energies (E_r) of each step for different paths in (001) and (100) surfaces are presented. The E_r of each step for each path corresponds to the reaction steps anatomized in Section S1.3.

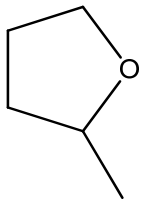
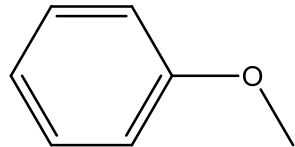
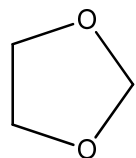
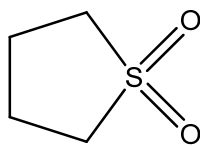
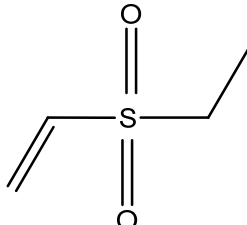
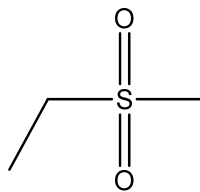
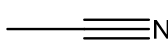
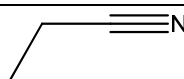
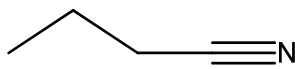
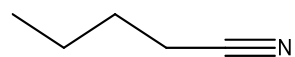
Reaction	E_r for (001) surface (eV)			E_r for (100) surface (eV)		
Step	Path 1	Path 2	Path 3	Path 1	Path 2	Path 3
1	-7.86	-1.52	-4.40	-7.76	-1.96	-5.83
2	0.89	-1.87	-0.85	0.43	-0.78	-2.83
3	-1.15	-2.36	-1.81	-2.22	-3.95	-1.44
4	-0.17	0.35	-2.10	-0.23	0.00	-1.92
5	-1.58	0.64	-0.37	-1.29	0.72	0.14
6	0.45	-5.11	-0.09	0.39	-5.52	0.41
7	-1.80	0.27	0.52	-2.06	-1.34	-0.26
8	-0.06	0.27	0.49	-0.39	0.66	0.39

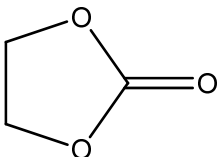
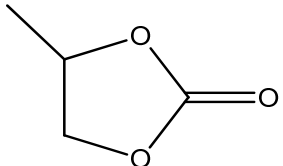
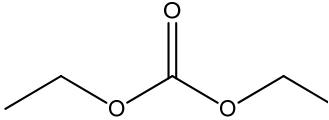
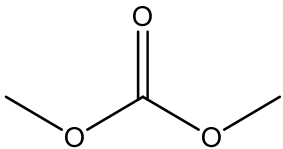
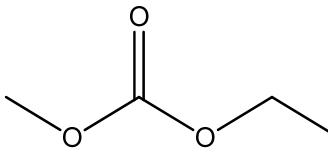
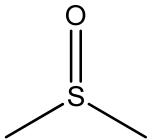
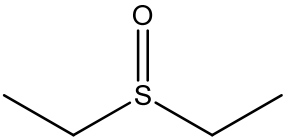
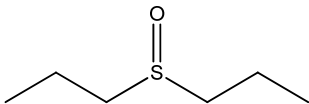
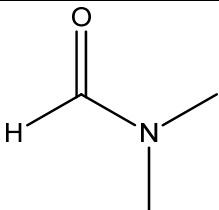
Table S3 The solvation free energy (ΔG_{sol}) of Li^+ and I^- in different solvents.

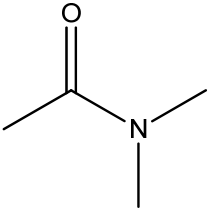
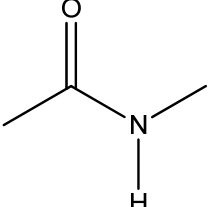
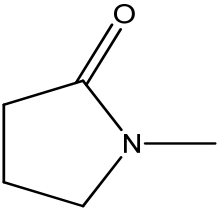
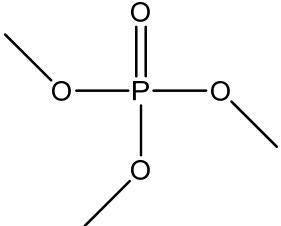
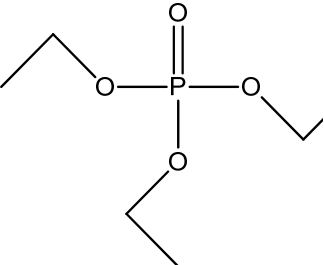
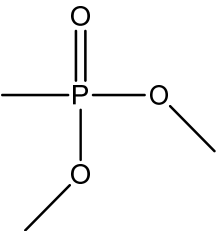
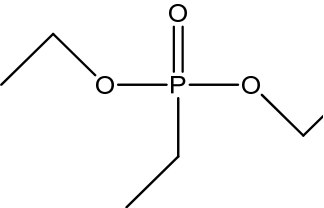
solvent	$\Delta G_{\text{sol}}(\text{Li}^+)$ (kJ/mol)	$\Delta G_{\text{sol}}(\text{I}^-)$ (kJ/mol)
DME	-585.534	-208.238
ACN	-613.772	-234.430
DMA	-625.956	-234.137
DMSO	-625.998	-233.969

Table S4 The 33 solvents investigated in the research. The E_b between solvent molecule and LiOH, as well as the bond length ($d_{\text{Li-O}}$) of the LiOH are tabulated.

type	solvent	schematics	E_b (eV)	$d_{\text{Li-O}}$ (Å)
LiOH	-	-	-	1.585
boron ester[41]	triol borate $\text{C}_5\text{H}_9\text{BO}_3$		0.638	1.618
	nitro-triol borate $\text{C}_4\text{H}_6\text{BNO}_5$		0.649	1.613
	diol-monoacid borate $\text{C}_5\text{H}_7\text{BO}_4$		0.615	1.610
	monoalcohol-diacid borate $\text{C}_5\text{H}_5\text{BO}_5$		0.491	1.607
	1,2-Dimethoxy ethane (DME) $\text{C}_4\text{H}_{10}\text{O}_2$		0.750	1.616
	Tetraethylene glycol dimethyl ether (TEGDME) $\text{C}_{10}\text{H}_{22}\text{O}_5$		0.749	1.615
Ether-based	Tetrahydrofuran (THF) $\text{C}_4\text{H}_8\text{O}$		0.831	1.619

Sulfone-based	2-methyl tetrahydrofuran (2-Me-THF) C ₅ H ₁₀ O[42]		0.850	1.619
	Methoxybenzene C ₇ H ₈ O[43]		0.654	1.612
	1,3-dioxolane(DOL) C ₃ H ₆ O ₂ [44]		0.690	1.611
	Tetraethylene sulfone (TMS) Sulfolane C ₄ H ₈ O ₂ S[45]		0.766	1.621
	ethyl vinyl sulfone (EVS) C ₄ H ₈ O ₂ S[46]		0.777	1.622
	ethyl methyl sulfone (EMS) C ₃ H ₈ O ₂ S[46]		0.772	1.620
Nitrile-based	Acetonitrile (ACN) C ₂ H ₃ N		0.799	1.618
	Propanenitrile C ₃ H ₅ N		0.820	1.621
	Butanenitrile C ₄ H ₇ N		0.830	1.621
	Pentanenitrile C ₅ H ₉ N		0.835	1.620

Carbonate-based	ethylene (EC) $C_3H_4O_3$	carbonate		0.774	1.620
	propylene (PC) $C_4H_6O_3$	carbonate		0.800	1.624
	diethyl (DEC) $C_5H_{10}O_3$	carbonate		0.834	1.623
	dimethyl (DMC) $C_3H_6O_3$	carbonate		0.799	1.621
	ethyl carbonate (EMC) $C_4H_8O_3$	methyl		0.818	1.622
Sulfoxide	Dimethyl sulfoxide (DMSO) C_2H_6OS			0.925	1.628
	Diethyl sulfoxide (DESO) $C_4H_{10}SO$			0.961	1.630
	Dipropyl sulfoxide (DPSO) $C_6H_{14}SO$			0.972	1.631
Amide-based	Dimethyl formamide (DMF) C_3H_7NO [47]			0.937	1.628

Dimethylacetamide (DMA) C_4H_9NO [47]		1.024	1.630
N-methylacetamide (NMA) C_3H_7NO [48]		0.983	1.630
N-methyl-2-pyrrolidone (NMP) C_5H_9NO [47]		0.990	1.630
Trimethyl phosphate (TMP) $C_3H_9PO_4$		0.978	1.630
Triethyl phosphate (TEP) $C_6H_{15}PO_4$		1.026	1.632
Dimethyl methylphosphonate (DMMP) $C_3H_9PO_3$		1.023	1.632
diethyl ethylphosphonate (DEEP) $C_6H_{15}PO_3$		1.055	1.633

Phosphate-based[49]

Table S5 Self-solvation free energies (kJ/mol) of the solvents predicted with different implicit models and the experimentally derived values, which are in perfect agreement with each other, confirming the reliability of the implicit SMD solvation model. The detailed deduction of the experimental self-solvation energy is shown in Section S1.6.

Solute/Solvent	Self-solvation free energy (kJ/mol)		
	SMD model ^a	Poisson-Boltzmann model ^[50]	Experimentally derived ^[51, 52]
ACN	−25.98	−25.0	−20.42
DMSO	−32.93	−34.9	−32.05
DMA	−30.50	−24.4	−28.58

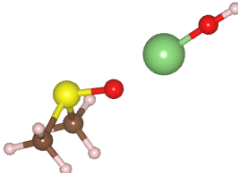
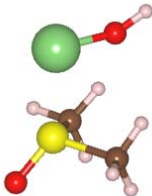
^a The structures and self-solvation free energy were obtained at the B3LYP/6-31g* and M05-2X/6-31g* level, respectively. The optimizations of the neutral solutes were conducted under the implicit SMD solvation model.

Table S6 The electronegativity of the correlated elements referenced in this work.^a

atom	Electronegativity (χ)
H	2.2
Li	0.98
B	2.04
C	2.55
N	3.04
O	3.44
P	2.19
S	2.58

^a<http://www.iun.edu/~cpanhd/periodictable.html>

Table S7 The binding energy (E_b) between the DMSO molecule and LiOH, with different atoms in DMSO bonding to LiOH. The color code is noted as: Li: green; O: red; H: pink; C: brown; S: yellow.

Hypothesized Bond	Optimized Structure ^a	E_b (eV)
O-Li		0.925
S-Li		0.588
C-Li	unstable	-
H-Li	unstable	-

^a The structures were optimized with DFT/PBE method.

Table S8 The desorption energy (E_{desorpt}) of lithium when binding with the solvent molecule in (100) surface and the binding energy (E_{b}) between LiOH molecule and the solvent molecule. The similar E_{desorpt} between the ACN and DMSO can be largely attributed to the hydrogen bonding between DMSO and the LiOH matrix, as shown in Fig. 4c and 4d.

solvent	E_{desorpt} (eV)	E_{b} (eV)
DME	7.187	0.978
ACN	6.988	1.035
DMSO	6.969	1.341

Table S9 The features for Machine Learning and the binding energy (E_b) between the solvent molecule and the LiOH are presented. In addition to the solvent property, the Highest Unoccupied Molecular Orbital (HOMO), Lowest Unoccupied Molecular Orbital (LUMO), and dipole moment (μ), the features of the functional group are formatted as site_atom, where the site is the atom site, dictated with three numbers, 0, 1, 2, representing the active center, the nearest coordinate site of the active center, the second nearest coordinate site of the active center, respectively. The value of site_atom is the electronegativity of the atom at the site multiplies the number of it. For example, 1_P is the electronegativity multiplies the number of it in the functional group and the number in the feature dictates that atom P is at the nearest coordination site of the active center. The 0_O, 0_N dictate the atom property of O and N at the active center, 1_B, 1_P, 1_C and 1_S dictate atom property of B, P, C and S at the nearest coordination sites, 2_N, 2_O, 2_C and 2_H dictate the atom property of N, O, C and H at the second nearest coordination sites.

solvent	Features													E_b (eV)
	HOMO (eV)	LUMO (eV)	μ (Debye)	0_O	0_N	1_B	1_P	1_C	1_S	2_N	2_O	2_C	2_H	
triol borate C ₅ H ₉ BO ₃	-6.81	-0.60	4.18	3.44	0.00	2.04	2.55	0.00	0.00	2.55	0.00	6.88	4.40	0.64
nitro-triol borate C ₄ H ₆ BNO ₅	-7.77	-2.76	0.09	3.44	0.00	2.04	2.55	0.00	0.00	2.55	0.00	6.88	4.40	0.65
diol-monoacid borate C ₅ H ₇ BO ₄	-7.75	-1.20	3.92	3.44	0.00	2.04	2.55	0.00	0.00	2.55	0.00	6.88	0.00	0.62
monoalcohol-diacid borate C ₅ H ₅ BO ₅	-8.26	-2.02	3.06	3.44	0.00	2.04	2.55	0.00	0.00	2.55	0.00	6.88	0.00	0.49
Dimethoy ethane C ₄ H ₁₀ O ₂	-7.02	1.28	0.00	3.44	0.00	0.00	5.10	0.00	0.00	2.55	0.00	0.00	11.00	0.75
Tetraethylene glycol dimethyl ether C ₁₀ H ₂₂ O ₅	-7.05	1.20	1.27	3.44	0.00	0.00	5.10	0.00	0.00	2.55	0.00	0.00	11.00	0.75
Tetrahydrofuran	-6.66	1.01	1.83	3.44	0.00	0.00	5.10	0.00	0.00	5.10	0.00	0.00	8.80	0.83

C ₄ H ₈ O														
	-6.69	1.06	1.67	3.44	0.00	0.00	5.10	0.00	0.00	7.65	0.00	0.00	6.60	0.84
2-methyltetrahydrofurane														
C ₅ H ₁₀ O[42]														
Methoxybenzene	-6.09	-0.21	1.36	3.44	0.00	0.00	5.10	0.00	0.00	5.10	0.00	0.00	6.60	0.65
C ₇ H ₈ O[43]														
1,3-dioxolane	-7.11	1.08	1.49	3.44	0.00	0.00	5.10	0.00	0.00	2.55	0.00	3.44	8.80	0.69
C ₃ H ₆ O ₂ [44]														
Tetraethylene sulfone	-7.79	0.42	5.61	3.44	0.00	0.00	0.00	0.00	2.58	5.10	0.00	3.44	0.00	0.77
C ₄ H ₈ O ₂ S[45]														
ethyl vinyl sulfone	-7.95	-1.37	4.98	3.44	0.00	0.00	0.00	0.00	2.58	5.10	0.00	3.44	0.00	0.78
C ₄ H ₈ O ₂ S[46]														
ethyl methyl sulfone	-7.97	0.42	5.00	3.44	0.00	0.00	0.00	0.00	2.58	5.10	0.00	3.44	0.00	0.77
C ₃ H ₈ O ₂ S[46]														
Acetonitrile	-9.14	0.72	3.86	0.00	3.04	0.00	2.55	0.00	0.00	2.55	0.00	0.00	0.00	0.80
C ₂ H ₃ N														
ethylene carbonate	-8.22	0.63	5.35	3.44	0.00	0.00	2.55	0.00	0.00	0.00	0.00	6.88	0.00	0.77
C ₃ H ₄ O ₃														
propylene carbonate	-8.14	0.63	5.50	3.44	0.00	0.00	2.55	0.00	0.00	0.00	0.00	6.88	0.00	0.80
C ₄ H ₆ O ₃														
diethyl carbonate	-7.86	1.08	0.55	3.44	0.00	0.00	2.55	0.00	0.00	0.00	0.00	6.88	0.00	0.83
C ₅ H ₁₀ O ₃														
dimethyl carbonate	-7.98	0.99	0.30	3.44	0.00	0.00	2.55	0.00	0.00	0.00	0.00	6.88	0.00	0.80

<chem>C3H6O3</chem>														
ethyl methyl carbonate	-7.92	1.04	0.46	3.44	0.00	0.00	2.55	0.00	0.00	0.00	0.00	6.88	0.00	0.82
<chem>C4H8O3</chem>														
Dimethyl sulfoxide	-6.28	0.73	4.15	3.44	0.00	0.00	0.00	0.00	2.58	5.10	0.00	0.00	0.00	0.92
<chem>C2H6OS</chem>														
Dimethyl formamide	-6.78	0.63	3.90	3.44	0.00	0.00	2.55	0.00	0.00	0.00	3.04	0.00	2.20	0.94
<chem>C3H7NO[47]</chem>														
Dimethylacetamide	-6.58	0.69	3.74	3.44	0.00	0.00	2.55	0.00	0.00	2.55	3.04	0.00	0.00	1.02
<chem>C4H9NO[47]</chem>														
N-methylacetamide	-6.83	0.76	3.73	3.44	0.00	0.00	2.55	0.00	0.00	2.55	3.04	0.00	0.00	0.98
<chem>C3H7NO[48]</chem>														
N-methyl-2-pyrrolidone	-6.57	0.74	3.82	3.44	0.00	0.00	2.55	0.00	0.00	2.55	3.04	0.00	0.00	0.99
<chem>C5H9NO[47]</chem>														
Trimethy phosphate	-8.07	0.87	2.78	3.44	0.00	0.00	0.00	2.19	0.00	0.00	0.00	10.32	0.00	0.98
<chem>C3H9PO4</chem>														
Triethyl phosphate	-7.94	0.74	3.03	3.44	0.00	0.00	0.00	2.19	0.00	0.00	0.00	10.32	0.00	1.03
<chem>C6H15PO4</chem>														
Dimethyl methylphosphate	-7.86	0.70	4.35	3.44	0.00	0.00	0.00	2.19	0.00	2.55	0.00	6.88	0.00	1.02
<chem>C3H9PO3</chem>														
diethyl ethylphosphonate	-7.69	0.78	2.36	3.44	0.00	0.00	0.00	2.19	0.00	2.55	0.00	6.88	0.00	1.06
<chem>C6H15PO3</chem>														
Propanenitrile	-9.01	0.35	3.95	0.00	3.04	0.00	2.55	0.00	0.00	2.55	0.00	0.00	0.00	0.82
<chem>C3H5N</chem>														
Butanenitrile	-8.94	0.46	4.07	0.00	3.04	0.00	2.55	0.00	0.00	2.55	0.00	0.00	0.00	0.83

C ₄ H ₇ N														
Pentanenitrile	-8.88	0.49	4.19	0.00	3.04	0.00	2.55	0.00	0.00	2.55	0.00	0.00	0.00	0.83
C ₅ H ₉ N														
diethyl sulphoxide	-6.14	0.58	3.98	3.44	0.00	0.00	0.00	0.00	2.58	5.10	0.00	0.00	0.00	0.96
C ₄ H ₁₀ OS														
Dipropyl sulfoxide	-6.10	0.62	3.85	3.44	0.00	0.00	0.00	0.00	2.58	5.10	0.00	0.00	0.00	0.97
C ₆ H ₁₄ OS														

References

- [1] M.J. Frisch, G.W. Trucks, H.B. Schlegel, G.E. Scuseria, M.A. Robb, J.R. Cheeseman, G. Scalmani, V. Barone, G.A. Petersson, H. Nakatsuji, X. Li, M. Caricato, A.V. Marenich, J. Bloino, B.G. Janesko, R. Gomperts, B. Mennucci, H.P. Hratchian, J.V. Ortiz, A.F. Izmaylov, J.L. Sonnenberg, Williams, F. Ding, F. Lipparini, F. Egidi, J. Goings, B. Peng, A. Petrone, T. Henderson, D. Ranasinghe, V.G. Zakrzewski, J. Gao, N. Rega, G. Zheng, W. Liang, M. Hada, M. Ehara, K. Toyota, R. Fukuda, J. Hasegawa, M. Ishida, T. Nakajima, Y. Honda, O. Kitao, H. Nakai, T. Vreven, K. Throssell, J.A. Montgomery Jr., J.E. Peralta, F. Ogliaro, M.J. Bearpark, J.J. Heyd, E.N. Brothers, K.N. Kudin, V.N. Staroverov, T.A. Keith, R. Kobayashi, J. Normand, K. Raghavachari, A.P. Rendell, J.C. Burant, S.S. Iyengar, J. Tomasi, M. Cossi, J.M. Millam, M. Klene, C. Adamo, R. Cammi, J.W. Ochterski, R.L. Martin, K. Morokuma, O. Farkas, J.B. Foresman, D.J. Fox, Gaussian 09, Revision D.01, Wallingford, CT, 2013.
- [2] D. Feller, The Role of Databases in Support of Computational Chemistry Calculations, *J. Chem. Phys.*, 17 (1996) 1571-1586, doi: 10.1002/(SICI)1096-987X(199610)17:13<1571::AID-JCC9>3.0.CO;2-P.
- [3] K.L. Schuchardt, B.T. Didier, T. Elsethagen, L. Sun, V. Gurumoorathi, J. Chase, J. Li, T.L. Windus, Basis Set Exchange: A Community Database for Computational Sciences, *J. Chem. Inf. Model.*, 47 (2007) 1045-1052, doi: 10.1021/ci600510j.
- [4] A.V. Marenich, C.J. Cramer, D.G. Truhlar, Universal Solvation Model Based on Solute Electron Density and on a Continuum Model of the Solvent Defined by the Bulk Dielectric Constant and Atomic Surface Tensions, *J. Phys. Chem. B*, 113 (2009) 6378-6396, doi: 10.1021/jp810292n.
- [5] G. Kresse, J. Furthmüller, Efficiency of ab-initio total energy calculations for metals and semiconductors using a plane-wave basis set, *Comput. Mater. Sci.*, 6 (1996) 15-50, doi: 10.1016/0927-0256(96)00008-0.
- [6] G. Kresse, J. Furthmüller, Efficient iterative schemes for ab initio total-energy calculations using a plane-wave basis set, *Phys. Rev. B*, 54 (1996) 11169-11186, doi: 10.1103/PhysRevB.54.11169.
- [7] G. Kresse, J. Hafner, Ab initio molecular dynamics for liquid metals, *Phys. Rev. B*, 47 (1993) 558-561, doi: 10.1103/PhysRevB.47.558.
- [8] G. Kresse, J. Hafner, Ab initio molecular-dynamics simulation of the liquid-metal--amorphous-semiconductor transition in germanium, *Phys. Rev. B*, 49 (1994) 14251-14269, doi: 10.1103/PhysRevB.49.14251.
- [9] P.E. Blöchl, Projector augmented-wave method, *Phys. Rev. B*, 50 (1994) 17953-17979, doi: 10.1103/PhysRevB.50.17953.
- [10] G. Kresse, D. Joubert, From ultrasoft pseudopotentials to the projector augmented-wave method, *Phys. Rev. B*, 59 (1999) 1758-1775, doi: 10.1103/PhysRevB.59.1758.
- [11] J.P. Perdew, K. Burke, M. Ernzerhof, Generalized Gradient Approximation Made Simple, *Phys. Rev. Lett.*, 77 (1996) 3865-3868, doi: DOI 10.1103/PhysRevLett.77.3865.
- [12] S. Grimme, J. Antony, S. Ehrlich, H. Krieg, A consistent and accurate ab initio parametrization of density functional dispersion correction (DFT-D) for the 94 elements H-Pu, *J. Chem. Phys.*, 132 (2010) 154104, doi: 10.1063/1.3382344.
- [13] P.W. Tasker, The stability of ionic crystal surfaces, *Journal of Physics C: Solid State Physics*, 12 (1979)

4977-4984, doi: 10.1088/0022-3719/12/22/036.

- [14] K.T. Butler, G. Sai Gautam, P. Canepa, Designing Interfaces in Energy Materials Applications with First-Principles Calculations, *npj Comput. Mater.*, 5 (2019) 19, doi: 10.1038/s41524-019-0160-9.
- [15] G. Scalmani, M.J. Frisch, Continuous surface charge polarizable continuum models of solvation. I. General formalism, *J. Chem. Phys.*, 132 (2010) 114110, doi: 10.1063/1.3359469.
- [16] V. Barone, M. Cossi, Quantum calculation of molecular energies and energy gradients in solution by a conductor solvent model, *J. Phys. Chem. A*, 102 (1998) 1995-2001, doi: 10.1021/jp9716997.
- [17] A. Klamt, V. Jonas, T. Burger, J.C.W. Lohrenz, Refinement and parametrization of COSMO-RS, *J. Phys. Chem. A*, 102 (1998) 5074-5085, doi: 10.1021/jp980017s.
- [18] L. Breiman, Arcing the edge, *Statistics*, 4 (1997) 1-14.
- [19] J.H. Friedman, Greedy function approximation: A gradient boosting machine, *Ann. Statist.*, 29 (2001) 1189-1232, doi: 10.1214/aos/1013203451.
- [20] J.H. Friedman, Stochastic gradient boosting, *Comput. Statist. Data Anal.*, 38 (2002) 367-378, doi: [https://doi.org/10.1016/S0167-9473\(01\)00065-2](https://doi.org/10.1016/S0167-9473(01)00065-2).
- [21] D.N. Theodorou, U.W. Suter, Detailed molecular structure of a vinyl polymer glass, *Macromolecules*, 18 (1985) 1467-1478, doi: 10.1021/ma00149a018.
- [22] D.N. Theodorou, U.W. Suter, Atomistic modeling of mechanical properties of polymeric glasses, *Macromolecules*, 19 (1986) 139-154, doi: 10.1021/ma00155a022.
- [23] M.P. Allen, D.J. Tildesley, *Computer Simulation of Liquids*, Oxford University Press, New York, 1987.
- [24] M. Ebrahimi, J.B. Hooper, D. Bedrov, Structural, Mechanical, and Dynamical Properties of Amorphous Li_2CO_3 from Molecular Dynamics Simulations, *Crystals*, 8 (2018) 473, doi: 10.3390/Cryst8120473.
- [25] S. Kurth, J.P. Perdew, P. Blaha, Molecular and solid-state tests of density functional approximations: LSD, GGAs, and meta-GGAs, *Int. J. Quantum Chem.*, 75 (1999) 889-909, doi: 10.1002/(sici)1097-461x(1999)75:4/5<889::aid-qua54>3.0.co;2-8.
- [26] M.W. Chase, *NIST-JANAF Thermochemical Tables*, American Institute of Physics: Melville, NY, 1998, doi: 10.18434/T42S31.
- [27] V.D. Parker, Energetics of Electrode Reactions. II. The Relationship between Redox Potentials, Ionization Potentials, Electron Affinities, and Solvation Energies of Aromatic Hydrocarbons, *J. Am. Chem. Soc.*, 98 (1976) 98-103, doi: 10.1021/ja00417a017.
- [28] O. Borodin, Molecular Modeling of Electrolytes, in: T.R. Jow (Ed.) *Electrolytes for Lithium and Lithium-Ion Batteries*, Modern Aspects of Electrochemistry, Springer Science+Business Media, New York, 2014, pp. 371-401.
- [29] C.P. Kelly, C.J. Cramer, D.G. Truhlar, Single-ion solvation free energies and the normal hydrogen electrode potential in methanol, acetonitrile, and dimethyl sulfoxide, *J. Phys. Chem. B*, 111 (2007) 408-422, doi: 10.1021/jp065403l.
- [30] O. Borodin, W. Behl, T.R. Jow, Oxidative Stability and Initial Decomposition Reactions of Carbonate, Sulfone, and Alkyl Phosphate-Based Electrolytes, *J. Phys. Chem. C*, 117 (2013) 8661-8682, doi: 10.1021/jp400527c.
- [31] C. Ling, R. Zhang, K. Takechi, F. Mizuno, Intrinsic Barrier to Electrochemically Decompose Li_2CO_3

-
- and LiOH, *J. Phys. Chem. C*, 118 (2014) 26591-26598, doi: 10.1021/jp5093306.
- [32] P. Winget, G.D. Hawkins, C.J. Cramer, D.G. Truhlar, Prediction of Vapor Pressures from Self-Solvation Free Energies Calculated by the SM5 Series of Universal Solvation Models, *J. Phys. Chem. B*, 104 (2000) 4726-4734, doi: 10.1021/jp992435i.
- [33] A.B. Owen, A robust hybrid of lasso and ridge regression, in: J.S. Verducci, X. Shen, J. Lafferty (Eds.) *Prediction and Discovery 2007*, pp. 59-71.
- [34] A.J. Smola, B. Scholkopf, A tutorial on support vector regression, *Statistics and Computing*, 14 (2004) 199-222, doi: 10.1023/b:stco.0000035301.49549.88.
- [35] Y. Liu, T. Zhao, W. Ju, S. Shi, Materials discovery and design using machine learning, *Journal of Materiomics*, 3 (2017) 159-177, doi: 10.1016/j.jmat.2017.08.002.
- [36] Y. Liu, B. Guo, X. Zou, Y. Li, S. Shi, Machine learning assisted materials design and discovery for rechargeable batteries, *Energy Storage Mater.*, 31 (2020) 434-450, doi: <https://doi.org/10.1016/j.ensm.2020.06.033>.
- [37] C. Chen, Y. Zuo, W. Ye, X. Li, Z. Deng, S.P. Ong, A Critical Review of Machine Learning of Energy Materials, *Adv. Energy Mater.*, 10 (2020), doi: 10.1002/aenm.201903242.
- [38] M. Bonomo, A. Carella, F. Borbone, L. Rosato, D. Dini, L. Gontrani, New pyran-based molecules as both n- and p-type sensitizers in semi-transparent Dye Sensitized Solar Cells, *Dyes Pigm.*, 175 (2020) 108140, doi: 10.1016/j.dyepig.2019.108140.
- [39] Y.G. Zhu, Q. Liu, Y. Rong, H. Chen, J. Yang, C. Jia, L.J. Yu, A. Karton, Y. Ren, X. Xu, S. Adams, Q. Wang, Proton enhanced dynamic battery chemistry for aprotic lithium-oxygen batteries, *Nat. Commun.*, 8 (2017) 14308, doi: 10.1038/ncomms14308.
- [40] W. Zhang, Y. Shen, D. Sun, Z. Huang, J. Zhou, H. Yan, Y. Huang, Promoting Li₂O₂ oxidation via solvent-assisted redox shuttle process for low overpotential Li-O₂ battery, *Nano Energy*, 30 (2016) 43-51, doi: 10.1016/j.nanoen.2016.09.031.
- [41] D. Shanmukaraj, S. Grugeon, G. Gachot, S. Laruelle, D. Mathiron, J.-M. Tarascon, M. Armand, Boron Esters as Tunable Anion Carriers for Non-Aqueous Batteries *Electrochemistry*, *J. Am. Chem. Soc.*, 132 (2010) 3055-3062, doi: 10.1021/ja9093814.
- [42] S.A. Freunberger, Y. Chen, N.E. Drewett, L.J. Hardwick, F. Barde, P.G. Bruce, The lithium-oxygen battery with ether-based electrolytes, *Angew. Chem. Int. Ed.*, 50 (2011) 8609-8613, doi: 10.1002/anie.201102357.
- [43] O. Crowther, B. Meyer, M. Salomon, Methoxybenzene as an Electrolyte Solvent for the Primary Lithium Metal Air Battery, *Electrochem. Solid-State Lett.*, 14 (2011) A113, doi: 10.1149/1.3596719.
- [44] D. Capsoni, M. Bini, S. Ferrari, E. Quartarone, P. Mustarelli, Recent advances in the development of Li-air batteries, *J. Power Sources*, 220 (2012) 253-263, doi: 10.1016/j.jpowsour.2012.07.123.
- [45] F. Wang, C.-S. Liang, Y. Pang, Y.-H. Xu, Z.-K. Luo, Electrochemical performance of a nonaqueous rechargeable lithium-air battery, *Ionics*, 19 (2013) 1791-1793, doi: 10.1007/s11581-013-0932-z.
- [46] F. Bardé, Y. Chen, L. Johnson, S. Schaltin, J. Fransaer, P.G. Bruce, Sulfone-Based Electrolytes for Nonaqueous Li-O₂ Batteries, *J. Phys. Chem. C*, 118 (2014) 18892-18898, doi: 10.1021/jp5048198.
- [47] Y. Chen, S.A. Freunberger, Z. Peng, F. Barde, P.G. Bruce, Li-O₂ Battery with a Dimethylformamide Electrolyte, *J. Am. Chem. Soc.*, 134 (2012) 7952-7957, doi: 10.1021/ja302178w.
- [48] V. Giordani, V.S. Bryantsev, J. Uddin, W. Walker, G.V. Chase, D. Addison, N-methylacetamide as an

Electrolyte Solvent for Rechargeable Li-O₂ Batteries: Unexpected Stability at the O₂ electrode, *ECS Electrochem. Lett.*, 3 (2013) A11-A14, doi: 10.1149/2.007401eel.

[49] Z.Q. Zeng, V. Murugesan, K.S. Han, X.Y. Jiang, Y.L. Cao, L.F. Xiao, X.P. Ai, H.X. Yang, J.G. Zhang, M.L. Sushko, J. Liu, Non-flammable electrolytes with high salt-to-solvent ratios for Li-ion and Li-metal batteries, *Nat. Energy*, 3 (2018) 674-681, doi: 10.1038/s41560-018-0196-y.

[50] D.G. Kwabi, V.S. Bryantsev, T.P. Batcho, D.M. Itkis, C.V. Thompson, Y. Shao-Horn, Experimental and Computational Analysis of the Solvent-Dependent O₂/Li⁺-O₂⁻ Redox Couple: Standard Potentials, Coupling Strength, and Implications for Lithium-Oxygen Batteries, *Angew. Chem. Int. Ed.*, 55 (2016) 3129-3134, doi: 10.1002/anie.201509143.

[51] A. Ben-Naim, Standard thermodynamics of transfer. Uses and misuses, *J. Phys. Chem.*, 82 (1978) 792-803, doi: 10.1021/j100496a008.

[52] A. Ben-Naim, Y. Marcus, Solvation thermodynamics of nonionic solutes, *J. Chem. Phys.*, 81 (1984) 2016-2027, doi: 10.1063/1.447824.